Energy 338 (2025) 138735

Contents lists available at ScienceDirect

Energy

journal homepage: www.elsevier.com/locate/energy

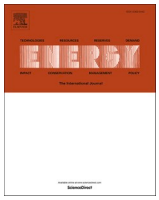

Synergistic heat recovery–dissipation architecture for hydrogen turbofans: Integrated heat current modeling with multi-parameter thermodynamic analysis

Weitong Liu [a,b], Guoqiang Xu [a,b], Xiuting Gu [a,b], Yiang Liu [a,b], Jiayang Wang [a,b], Jingzhi Zhang [c], Yanchen Fu [a,b,*]

[a] Research Institute of Aero-engine, Beihang University, Beijing, 100191, China
[b] Tianmushan Laboratory, Hangzhou, 310023, China
[c] School of Nuclear Science, Energy and Power Engineering, Shandong University, Jinan, 250061, Shandong, China

ARTICLE INFO

Handling Editor: Ruzhu Wang

Keywords:
Hydrogen turbofan engine
Thermal management system
Intermediate cycle heat exchange
Energy-flow modeling

ABSTRACT

Hydrogen-fueled aero engines offer a promising path toward decarbonizing aviation, but their adoption is hindered by the dual challenges of safely preheating cryogenic liquid hydrogen (LH_2) and efficiently recovering onboard waste heat. Most studies focus on components or simplified models, overlooking phase-change effects and intermediate-cycle integration. Moreover, conventional mass-flow-based modeling introduces excessive intermediate variables, limiting efficiency and applicability in complex hydrogen turbofan systems. To address these gaps, this study proposes a novel synergistic heat recovery–dissipation architecture for hydrogen turbofan engines, incorporating four functional heat exchangers and a helium-based intermediate cycle. Besides, a novel energy-flow-oriented thermal modeling framework based on the heat current method is developed, coupled with a phase-change LH_2 preheating model. The model is validated against published data, yielding a temperature deviation below 23.15 K. Parametric analyses reveal that increasing turbine inlet temperature enhances heat transfer performance and thrust, while optimal values of bypass ratio ($B = 2.4$) and helium flow distribution ($\phi = 0.7$) maximize thermal efficiency and preheated hydrogen temperature. Additionally, the helium mass flow rate and its distribution ratio provide effective yet saturable control over heat exchanger performance. These results demonstrate the viability of integrating intermediate-cycle systems into hydrogen turbofans and highlight the advantages of energy-flow-based modeling in reducing system complexity while capturing nonlinear thermal behavior. The proposed architecture and methodology provide new insights into the design of advanced thermal management systems and support the development of high-performance, zero-emission aviation propulsion technologies.

Nomenclature

A	heat transfer area of HEX [m^2]
B	bypass ratio
c_p	isobaric specific heat capacity [J/(kg·K)]
F	thrust [kN]
F_s	specific thrust [(N·s)/kg]
G	heat capacity flow rate [J/(K·s)]
H	flight altitude [m]
h	specific enthalpy [J/kg]
K	overall heat transfer coefficient [W/(m^2·K)]
KA	thermal conductivity of HEX [W/K]

(*continued on next column*)

(*continued*)

k	specific heat ratio of air
k_g	specific heat ratio of exhaust gas
L_v	latent heat of vaporization of hydrogen [J/kg]
M	molar mass [g/mol]
Ma	Mach number
m	mass flow rate [kg/s]
P	pressure [Pa]
Q	heat transfer rate [kW]
R	inlet temperature difference-based thermal resistance [K/W]
T	temperature [K]
W	compression or expansion work [kW]

(*continued on next page*)

* Corresponding author. Research Institute of Aero-engine, Beihang University, Beijing, 100191, China.
E-mail address: yanchenfu@buaa.edu.cn (Y. Fu).

https://doi.org/10.1016/j.energy.2025.138735
Received 26 May 2025; Received in revised form 11 September 2025; Accepted 29 September 2025
Available online 3 October 2025

(*continued*)

Greek symbols	
ϵ	thermal-motive force [K]
δ_{HPC}	compressor bleed air ratio
π	pressure ratio
η	efficiency
σ	pressure recovery factor
ϕ	distribution ratio of helium flow in branches
Subscripts	
CA	turbine cooling air
Cal	calculated data
c	cold-side fluid
core	core engine
evapor	evaporation
gas	exhaust gas
He	helium
H_2	hydrogen
h	hot-side fluid
in	inlet
min	minimum
Ref	reference data
sup	superheating
th	thermal
Abbreviations	
AFR	air-to-fuel ratio
ATI	Aerospace Technology Institute
CCA	Cooled Cooling Air
CC	combustion chamber
EDN	exhaust nozzle
FDN	fan nozzle
FCR	fuel cost rate [$/s]
HEX	heat exchanger
HySIITE	Hydrogen Steam and Inter-Cooled Turbine Engine
HPC	high-pressure compressor
HPT	high-pressure turbine
ICAO	International Civil Aviation Organization
LH_2	liquid hydrogen
LPC	low-pressure compressor
LPT	low-pressure turbine
LHV	lower heating value [kJ/kg]
SOFC	Solid Oxide Fuel Cell
SABRE	Synergistic Air-Breathing Rocket Engine
SFC	specific fuel consumption [kg/(N·h)]
SFCR	specific fuel cost rate [$/(kN·s)]
TMS	thermal management system

1. Introduction

With the transformation of global energy structures and the increasing demand for environmental protection, hydrogen, as a clean and efficient energy carrier, is gradually gaining attention in the aviation sector. The International Civil Aviation Organization (ICAO) Committee on Aviation Environmental Protection forecasts that CO_2 emissions will increase by 21 % in 2040 relative to the base year of 2015 [1,2]. Research by Oesingmann et al. [3] predicts that by 2050, the aviation industry's demand for liquid hydrogen could reach 17 million tons, resulting in a 9 % reduction in global aviation CO_2 emissions. Hydrogen aviation propulsion systems, characterized by their zero-carbon emissions and high energy density of 120 MJ/kg—approximately three times that of aviation kerosene—are regarded as pivotal technologies for achieving sustainable development in the aviation industry. However, hydrogen-fueled aero engines confront two critical thermal management challenges that significantly impede their widespread implementation. The first is the requirement of cryogenic liquid hydrogen (LH_2) vaporization. The utilization of LH_2 with its ultralow boiling point (20.37 K at 1 atm [4]) demands sophisticated preheating systems. This stored cryogenic fuel must undergo phase transition through heat exchangers (HEX) before entering combustion chambers [5].The second is the efficient cold energy utilization. Effective cascade utilization of high-grade cold energy through thermodynamic cycle integration is crucial for maximizing overall engine efficiency and power density enhancement.

An efficient TMS ensures the safety and operational efficiency of hydrogen across different flight conditions, directly influencing the performance and economic viability of aero engines. There are various methods for utilizing LH2's cold energy to enhance aero-engine performance, such as cooling of ram air [6,7], compressed air [8], turbine cooling air [9], oil [10], and exhaust gas [11,12]. In 2022, Pratt & Whitney introduced the Hydrogen Steam and Inter-Cooled Turbine Engine (HySIITE) concept [13], in which LH_2 exchanges heat solely with gas in the HEX at the exhaust nozzle to generate steam. This cooled, liquefied water is then heated in the evaporative HEX, and the resulting vaporized steam is injected into the intercooler and combustion chamber, reducing flame temperature and NO_x emissions. The European ENABLEH2 hydrogen turbofan project integrates four HEXs, each with distinct functions, into the TMS to facilitate hydrogen's precooling, intercooling, and regeneration processes [14]. This architecture improves the engine's thermal efficiency and lowers the temperature in the combustor [1]. However, in this configuration, hydrogen directly exchanges heat with high-temperature air or gas. Led by the Aerospace Technology Institute (ATI), which is funded by the UK government, the FlyZero project [15] represented a significant advancement toward zero-carbon emission in commercial aviation [15]. It highlighted the potential for integrating exhaust gas heat recovery into the engine as early as 2026 [16]. Nonetheless, direct heat exchange between extremely cold hydrogen and high-temperature exhaust gas (700–800 K [17]) could result in considerable exergy losses due to the vast temperature difference. Patrao et al. [18] investigated the performance of the intercooled-recuperated hydrogen engine concepts, finding that this layout improves the take-off specific fuel consumption with a reduction of up to 7.7 % compared to the baseline uncooled engine. Seitz et al. [19] proposed a hybrid hydrogen engine concept featuring a Solid Oxide Fuel Cell (SOFC) and a turbine engine operating independently. This design utilizes a condenser to recover water vapor from the exhaust gases of the fuel cell and injects it into the combustor to enhance thermal efficiency and reduce NO_x emissions. Berg et al. [6] conducted systematic design and performance analysis studies on TMS for hydrogen-fueled distributed aircraft propulsion system. They proposed a scheme featuring a primary precooler that uses LH_2 and introduces a helium intermediate cycle heat exchange system. Liu et al. [5] developed a combined power generation TMS featuring both hydrogen direct expansion and Rankine cycles to simultaneously utilize the cold exergy from LH_2 and the heat exergy from the exhaust gas of a hydrogen turbojet engine.

Current research and development of hydrogen-fueled aero engines primarily focus on adaptive modification of existing engine models. The substitution of conventional aviation kerosene with hydrogen has induced significant alterations in thermodynamic characteristics, economic performance, and sustainability of propulsion systems, where these transformations are being actively investigated within academic circles. Balli et al. [20] presented a detailed thermodynamic analysis of the TF33 turbofan engine when operated with hydrogen gas compared to aviation kerosene. The findings demonstrate that fuel mass flow rate and specific fuel consumption drop by 63.83 % and 60.61 %, respectively, while engine thrust slightly decreases and fuel cost rate increases by 290.91 %. Akdeniz and Balli [21] performed a comparative analysis of the thermodynamic characteristics of the high bypass turbofan engine PW4056, comparing hydrogen fuel to aviation kerosene. The results indicated that hydrogen fuel reduced the engine's overall exergy efficiency from 26.9 % to 24.3 %. Regardless of the fuel type, the combustor consistently showed the lowest exergy efficiency, recording 58.20 % with hydrogen and 64.24 % with aviation kerosene. Oğur et al. [22,23] presented a comprehensive analysis of the thermodynamic performance of the GEnx-ib76 turbofan engine, fueled by both hydrogen and kerosene at various altitudes. Results reveal that hydrogen-fueled engines provide higher thrust at takeoff but reduced thrust during cruise, attributed to a lower fuel mass flow rate. Despite higher operating costs, hydrogen offers a sustainable alternative to kerosene, owing to its lower

environmental impact. The thermodynamic performance of the GE90 engine using hydrogen fuel was studied by Derakhshandeh et al. [24], and similar conclusions were drawn as mentioned above. However, the hydrogen fuel used in these comparative studies was in gaseous rather than liquid form. These studies overlooked the preheating and vaporization of cryogenic LH_2 and the utilization of its cold energy, thereby limiting the scope of their conclusions.

For hydrogen-fueled aero engines, ensuring safe and efficient heat exchange is crucial for both preheating cryogenic LH_2 and utilizing its cold energy. Due to its flammability and explosiveness, safety concerns pose a significant barrier to the use of hydrogen. The aero-engine HEX operates under fluctuating loads [25], increasing the risk of damage to the heat exchange unit. Consequently, direct heat transfer between LH_2 and high-temperature air could present a fire hazard if the heat exchange components fail. To address the limitations of direct heat exchange between aviation fuel and high-temperature air, researchers have proposed an intermediate cycle heat exchange system. This system uses a safe, reliable third fluid to indirectly transfer heat between the fuel and high-temperature air through separate HEXs in the intermediate cycle [26,27]. In the early 1990s, Reaction Engines Limited introduced the Skylon project [28], which featured the innovative Synergistic Air-Breathing Rocket Engine (SABRE) concept [29]. A defining characteristic of the SABRE is its advanced intermediate cycle heat exchange system, comprising three distinct HEXs [30]. This system primarily relies on low-temperature LH_2 as a heat sink for cooling both ram air and high-temperature gases. However, by incorporating helium as an intermediate working fluid in a closed-loop cycle, the system facilitates the indirect transfer of heat. The use of this third fluid indirectly heat exchange approach not only enhances the engine's thermal efficiency but also mitigates challenges such as hydrogen embrittlement and the safety concerns associated with precoolers. Throughout the development of SABRE, it progressed through the SABRE-3 [31], SABRE-4 [32], and Scimitar [33] designs, each incorporating intermediate cycle heat exchange systems. Recently, Cheng et al. [34] introduced a fuel-based indirect cooling TMS for hydrocarbon-fueled scramjet that uses liquid metal as the intermediate working medium and assessed its thermal performance. As for hydrocarbon-fueled turbofans, Liu et al. [26] proposed a multilevel heat exchange system with multifluid that simultaneously achieves fuel preheating, bearing chamber cooling air cooling, and compressor bleed air cooling. Through experimental research and theoretical modeling, Liu et al. [35] achieved the system thermodynamic parameter prediction error of less than 10 %. Fu et al. [36] proposed a theoretical optimization model to optimize the heat transfer area of the intermediate cycle heat exchange system in aero engines, with the goal of reducing the TMS's weight. Liu et al. [37,38] explored the simulation and optimization of an aero-engine TMS with intermediate cycles, utilizing an artificial neural network and the heat current method.

Overall, given the numerous advantages of intermediate cycle heat exchange, incorporating such systems into aero-engine TMS is becoming increasingly important [39]. Particularly for hydrogen turbofans, where intermediate cycle heat exchange is crucial for LH_2 preheating, tiered energy utilization, and ensuring the safety of the heat transfer process. However, existing research on hydrogen-fueled aero engines typically overlooks the phase change heat transfer of LH_2, focusing instead on component-level design, such as the hydrogen combustion chamber or HEXs. Thus, the current research gap lies in the integration of intermediate cycle heat exchange systems into hydrogen-fueled propulsion systems, enabling efficient and safe heat recovery and dissipation in the thermal management system.

Moreover, to investigate the thermodynamic characteristics and overall performance of hydrogen turbofans, developing an efficient modeling approach is essential. Current thermodynamic modeling often uses the sequential modular approach, which divides the system into components and builds a mathematical model by stacking the governing equations of each [40]. However, this method is based on mass flow topology and involves lots of constraints and variables, introducing unnecessary intermediate variables that complicate the analysis and solution of complex systems. This is particularly challenging for hydrogen turbofans, as the highly complex TMS, which integrates an intermediate cycle heat exchange system with multiple components, multi-parameter coupling, and strong non-linearity, leads to high computational demands and significantly increased computation time [41,42]. Using the radiation-network method and thermo-electrical analogy, Chen et al. [43,44] innovatively defined the thermal resistance of HEXs based on inlet temperature differences and developed the heat current method. This method, grounded in energy flow topology, facilitates the modeling of various energy transfer processes within thermal systems and the reduction of unnecessary intermediate variables [45]. Currently, the heat current method has been successfully applied in lots of fields such as SOFC cogeneration systems [46], absorption energy storage systems [47], district heating systems [48], liquid desiccant dehumidification process [49], thermal power conversion systems [50], and so on. Therefore, considering the multi-parameter coupling and the phase change heat transfer process of LH_2, the heat current method provides an alternative solution for the thermodynamic modeling of hydrogen turbofans.

This paper presents a novel synergistic heat recovery-dissipation architecture for a hydrogen turbofan, integrating four HEXs serving different functions to achieve efficient, tiered utilization of the engine's energy flow. Unlike conventional mass-flow-based modeling, this work innovatively conducts energy-flow-oriented thermal modeling of the hydrogen-fueled engine and integrates a LH_2 phase change preheating model based on the heat current method. The model's accuracy was validated through comparison with existing literature data. Additionally, this study investigates the effects of bypass ratio, turbine inlet temperature, helium mass flow rate, and helium flow distribution ratio on the thermodynamic characteristics of hydrogen turbofan.

2. Architecture description

The schematic diagram of the proposed synergistic heat recoverydissipation architecture for hydrogen turbofan engines is depicted in Fig. 1, consisting of the typical turbofan engine, the intermediate cycle heat exchange system, and a recuperator (HEX-4). The function of this thermal management architecture is to preheat cryogenic LH_2 before combustion while dissipating onboard heat loads, and to recover waste heat from the exhaust gases, thereby facilitating efficient tiered utilization of the engine's overall energy flow. Considering helium's chemical inertness, high thermal conductivity, and stability under extremely low-temperature conditions, helium has been chosen as the working fluid for the intermediate cycle to ensure the safety and stability of the TMS. HEX-1 is an air−helium intercooler that lowers the inlet air temperature and thermal load of the high-pressure compressor (HPC), thereby reducing the rotor power consumption. HEX-2, a compressor bleed air−helium HEX, functions as a Cooled Cooling Air (CCA) cooler, improving the quality of turbine cooling air and allowing for higher turbine inlet temperature [51,52]. HEX-3 is a LH_2−helium preheater, which fully vaporizes the LH_2 and heats it to a temperature suitable for combustion. HEX-4, an air−exhaust gas recuperator, recovers waste heat from the low-pressure turbine (LPT) exhaust and raises the combustion chamber (CC) air inlet temperature, thus decreasing the specific fuel consumption (*SFC*). Additionally, the use of the intercooler increases the temperature difference in the recuperator, enhancing heat exchange efficiency and further recovering waste heat. Besides, all HEXs are of the counterflow type. Cryogenic LH_2 is the terminal heat sink to cool the high-temperature air and exhaust gas.

The proposed hydrogen turbofan engine features a sperate-flow turbofan configuration, and its operation process is described as follows. Air entering through the intake is initially compressed by the fan (1−1.0) and then split into two streams: the bypass and the core flow. The bypass flow is expelled directly through the fan nozzle (FDN),

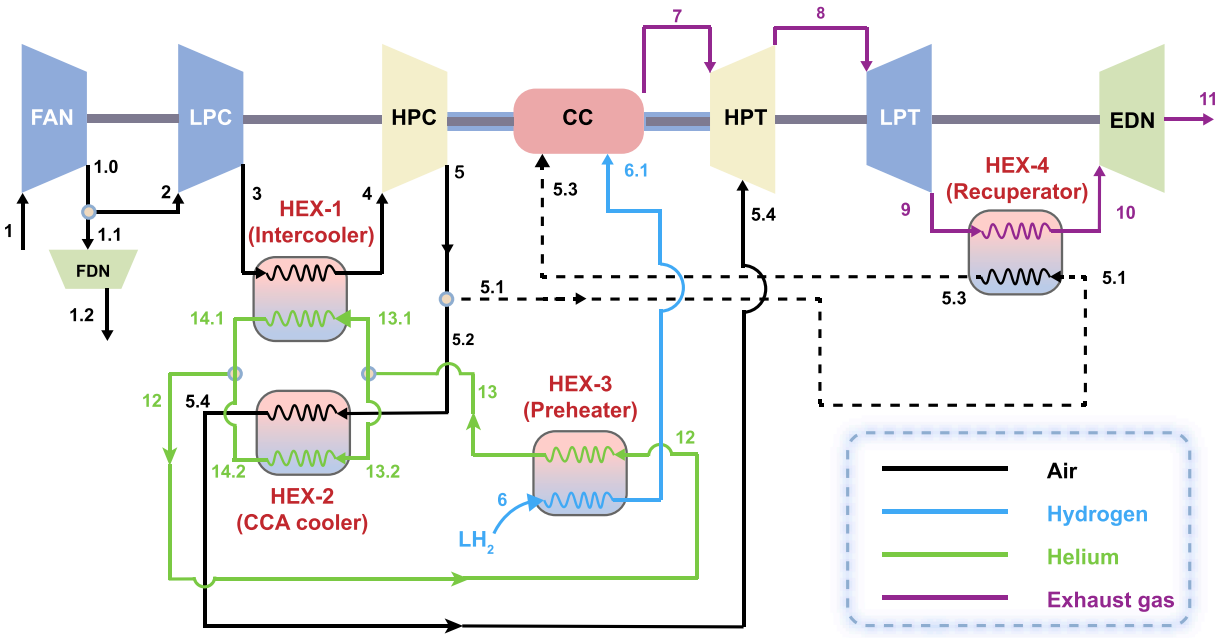

Fig. 1. Schematic diagram of the synergistic heat recovery-dissipation architecture for hydrogen turbofan engines.

contributing to thrust generation (1.1−1.2); meanwhile, the core flow undergoes initial compression (2−3) in the low-pressure compressor (LPC), passes through HEX-1 for heat exchange (3−4), and subsequently is further compressed by HPC (4−5). Afterward, the air is divided into two paths. One path, the compressor bleed air, passes through HEX-2 for heat exchange (5.2−5.4) before entering the high-pressure turbine (HPT). The other path undergoes heat exchange in HEX-4 (5.1−5.3), then enters the CC where it mixes with hydrogen and combusts to generate high-temperature gas. This gas then sequentially flows through the HPT (7−8) and LPT (8−9), expanding and performing work. The turbines drive the compressors through the shaft system. Finally, after heat exchange in HEX-4 (9−10), the high-temperature gas is expelled through the exhaust nozzle (EDN), generating additional thrust. HEX-1, HEX-2, and HEX-3 are interconnected through the helium pathway. HEX-1 and HEX-2 are situated on parallel branches, whereas HEX-3 is positioned along the main flow path. In the conceptual design of this study, the helium cycle is driven by a helium compressor, which in turn is powered by a helium turbine. This can be realized in two ways: (i) Turbine-compressor arrangement. After helium absorbs heat in HEX-1 and HEX-2, its temperature and enthalpy increase. By placing a helium turbine upstream of HEX-3, the helium expansion can drive a turbine coaxially coupled with the helium compressor, thereby sustaining the circulation loop. This arrangement concept is similar to the SABRE scheme [30]. (ii) Electric motor arrangement. Considering that hybrid power architectures are an important development direction for hydrogen-fueled aero engines, the helium turbine can alternatively be driven by an electric motor powered by a SOFC, providing auxiliary power and improved controllability. However, the main objective of this work is to investigate energy-flow modeling and to analyze the effects of thermodynamic parameters on overall system performance. For this reason, the detailed compressor drive configuration was not the focus of the present analysis.

Considering the advanced technology of the F-119 engine and the widespread application of the TF33 engine, the main parameters of the proposed hydrogen turbofan engine incorporate design parameters from both engines [20,53]. The selected design point targets sea-level-static conditions, with engine specifications detailed in Table 1 [23,54].

Table 1
The proposed hydrogen turbofan engine specifications [23,54].

Parameter	Value	Parameter	Value
Air mass flow rate	150 kg/s	Mechanical efficiency (η_m)	0.99
Bypass ratio (B)	1.2	Combustion efficiency (η_{CC})	0.99
Pressure ratio of FAN (π_{FAN})	1.77	CC pressure recovery factor (σ_{CC})	0.94
Pressure ratio of LPC (π_{LPC})	2.42	HEX pressure recovery factor (σ_{HEX})	0.95
Pressure ratio of HPC (π_{HPC})	5.8	Compressor bleed air ratio (δ_{HPC})	0.1
Fan isentropic efficiency ($\eta_{FAN,s}$)	0.93	Hydrogen mass flow rate (m_6)	1 kg/s
Compressor isentropic efficiency ($\eta_{C,s}$)	0.91	Helium mass flow rate (m_{12})	0.8 kg/s
Turbine isentropic efficiency ($\eta_{T,s}$)	0.93	Distribution ratio of helium flow in branches (ϕ)	0.8

Note: The baseline parameters are initial design values. In particular, $\phi = 0.8$ was preliminarily set by engineering judgment, since the intercooler typically handles a significantly larger heat load than the CCA cooler.

3. Energy-flow oriented thermal modeling

An effective modeling approach is crucial for directly comprehending and assessing the thermodynamic performance of hydrogen turbofan engines. Unlike conventional methods that rely on mass flow topology for modeling, this study utilizes the heat current method [45] to conduct thermal modeling of hydrogen-fueled aero engines oriented towards energy flow. The overall modeling framework is summarized in Fig. 2. The model consists of four main parts: component modeling, phase-change coupled LH_2 preheating modeling, heat current model of the engine, and engine governing equations. A detailed description of each module and the governing equations are provided in the following subsections. To simplify the analysis, assumptions made in the current study are listed below [55].

(1) Every component maintains equilibrium and remains in a steady state.
(2) The compressors (FAN, LPC, HPC), combustion chamber, and turbines (HPT, LPT) are considered to operate adiabatically.

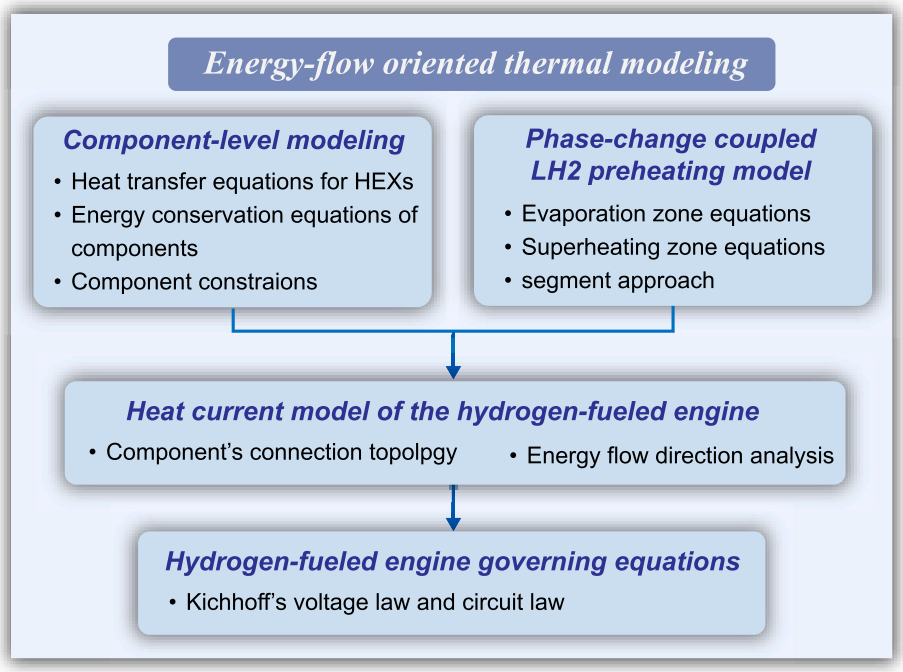

Fig. 2. The block diagram of the energy-flow oriented thermal modeling.

(3) Heat losses in all HEXs and pipelines are ignored, and pressure drops in pipelines are neglected.
(4) Both air and exhaust gases are assumed to be ideal gases.
(5) A completed combustion process is considered and the lower heating value (*LHV*) is taken as 119450 kJ/kg for hydrogen fuel.
(6) Except for HEX-3, the thermal properties of the working fluids flowing through each component are determined by its average temperature and pressure.
(7) The liquid hydrogen entering HEX-3 is in a saturated state, with its temperature (saturation temperature, $T_{saturation}$) determined by its pressure.
(8) The energy impact of the helium compressor and helium turbine driving the helium cycle is neglected.

These assumptions simplify the model but inevitably reduce fidelity in representing real engine behavior. For steady-state operation, neglecting transient effects may underestimate the dynamic mismatch between cooling demand and available capacity during rapid load changes. Therefore, the model is not applicable to dynamic engine analyses. Regarding the neglect of heat losses and pipeline pressure drops, this may slightly overestimate heat exchanger effectiveness and flow performance. However, for specific applications, heat loss coefficients and pressure drops can be incorporated as correction factors to align the model with actual engine performance. As for the assumption of constant thermal properties, since the properties of air and helium vary nearly linearly under the studied conditions, and segmented treatment is applied to liquid hydrogen heat exchange, the impact of this assumption on predictive accuracy is very limited.

3.1. Global heat current network topology

For a counterflow HEX with constant properties and no phase change, by combining the heat transfer equation with the energy conservation equation, the inlet temperature difference-based thermal resistance of the heat exchanger can be derived [43]:

$$R=\frac{T_{h,in}-T_{c,in}}{Q}=\frac{G_c\exp\left(\frac{KA}{G_h}\right)-G_h\exp\left(\frac{KA}{G_c}\right)}{G_hG_c\left[\exp\left(\frac{KA}{G_h}\right)-\exp\left(\frac{KA}{G_c}\right)\right]} \quad (1)$$

where T is the temperature, Q is the heat transfer rate, K is the overall heat transfer coefficient, A is the heat transfer area, KA is the thermal conductivity of HEX, G represents the fluid heat capacity flow rate, i.e., the product of mass flow rate and isobaric specific heat capacity, subscripts 'h' for hot-side fluid, 'c' for cold-side fluid, 'in' for inlet.

The temperature of a single working medium changes through heat exchange or thermodynamic conversion processes such as compression, expansion, and throttling. These temperature changes can be described by thermal-motive forces ε, specifically the differences between node temperatures, which are determined by the energy conservation relationships and constraint equations. Using these fundamental relationships, the global heat current network of the proposed synergistic heat recovery-dissipation architecture for hydrogen turbofan engines has been constructed, as illustrated in Fig. 3. Based on the thermoelectric analogy, Fig. 3 presents the heat current network of the engine, which intuitively demonstrates the energy flow of the engine. As for the LH_2 preheater HEX-3, where LH_2 undergoes evaporation and superheating, leading to significant changes in its thermophysical properties, these processes can be segmented to ensure the applicability of Eq. (1).

In the heat current model of the hydrogen turbofan engine shown in Fig. 3, the thermal-motive force, ε, represents the temperature changes of the fluid caused by heat exchange, compression, or expansion processes. Q_i and R_i respectively denote the heat transfer rate and thermal resistance within each HEX, while Q_{CC} indicates the heat released by hydrogen combustion. Additionally, in the fan and compressor, air is compressed and absorbs energy; conversely, in the turbine, the expanding gas performs work and releases energy. Consequently, energy sources, W_i, are introduced to represent the work inputs and outputs. Based on the above analysis, the constructed heat current model clearly illustrates the energy transport process in the hydrogen turbofan engine: thermal loads enter the system from multiple boundary nodes, transfer to the LH_2 through the helium intermediate heat exchange cycle and

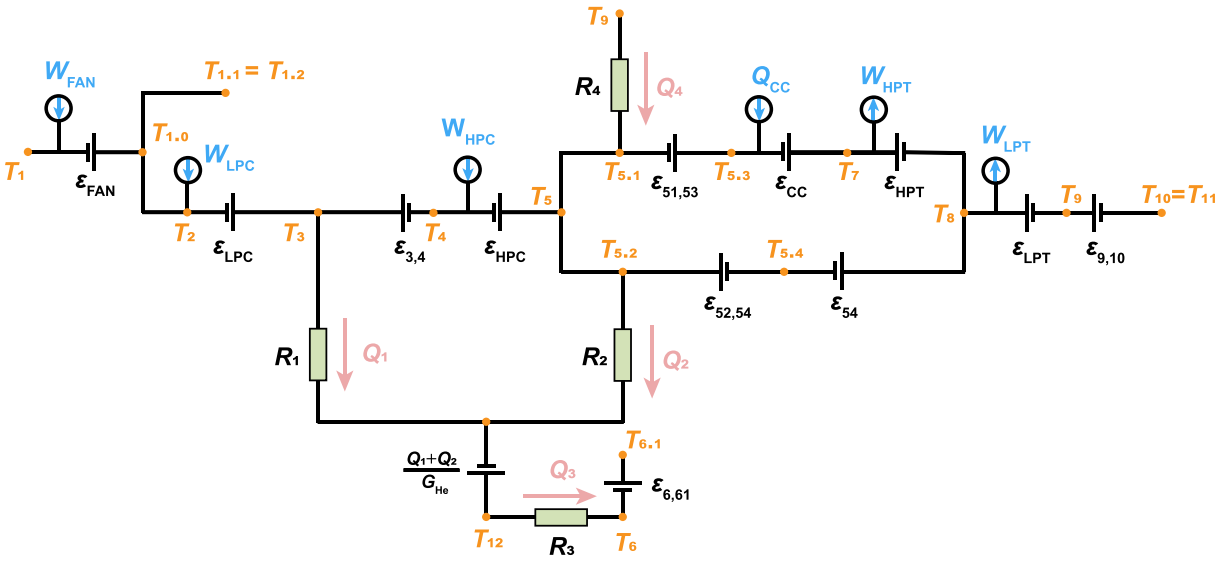

Fig. 3. Heat current model of the synergistic heat recovery-dissipation architecture for hydrogen turbofan engines.

heat transfer processes, and finally exit at node 11. Applying Kirchhoff's voltage law to the heat current model yields the overall constraint equations that describe the heat transport and conversion processes within the system, as shown in the following subsections. During the thermodynamic calculation and analysis process, the thermal properties of all working fluids are obtained from the open-source thermophysical property library CoolProp [56].

Unlike the sequential modular approach commonly used in the literature for aero-engine thermodynamic modeling [10,40], the abovementioned energy-flow oriented thermal modeling method based on global heat current network topology facilitates the modeling of various energy transfer processes, reduces unnecessary intermediate variables, and enhances computational efficiency.

3.2. Component-level modeling

(1) Environment and Intake

The inlet conditions are defined using the standard atmospheric model [14], with flight altitude (H) and Mach number (Ma) provided as inputs. The atmospheric temperature (T_0) and pressure (P_0) are initially determined based on the altitude, as shown in Eqs. (2) and (3):

$$T_0 = \begin{cases} 288.15 - 0.0065H & H \le 11000\text{m} \\ 216.7 & H > 11000\text{m} \end{cases} \tag{2}$$

$$P_0 = \begin{cases} 101325 \times \left(1 - \dfrac{H}{44308}\right)^{5.2553} & H \le 11000\text{m} \\ 22700e^{\frac{11-H/1000}{6.338}} & H > 11000\text{m} \end{cases} \tag{3}$$

Given Ma, the inlet total temperature (T_1) and total pressure (P_1) are:

$$T_1 = T_0\left(1 + \frac{k-1}{2}Ma^2\right) \tag{4}$$

$$P_1 = P_0\left(1 + \frac{k-1}{2}Ma^2\right)^{\frac{k}{k-1}} \tag{5}$$

where k is the specific heat ratio, equal to 1.4 for air.

(2) FAN and FDN

FAN is a compression component, with the pressure ratio and isentropic efficiency specified as input parameters at the design point. Based on Fig. 3 and the first law of thermodynamics, the following constraint equation must be satisfied:

$$m_{1.0} = m_1 \tag{6}$$

$$\varepsilon_{\text{FAN}} = T_{1.0} - T_1 = T_1\left(\pi_{\text{FAN}}^{\frac{k-1}{k}} - 1\right) \Big/ \eta_{\text{FAN,s}} \tag{7}$$

$$W_{\text{FAN}} = G_1(T_{1.0} - T_1) \tag{8}$$

$$P_{1.0} = \pi_{\text{FAN}} P_1 \tag{9}$$

where m is the mass flow rate, and the subscripts indicate the node positions, as shown in Fig. 1.

The airflow compressed by the FAN is directed into both the core and bypass ducts. The bypass airflow is discharged through the FDN. Since the expansion ratio of the FDN is relatively small and can be neglected, the inlet and outlet parameters satisfy the following relationship:

$$m_{1.2} = m_{1.1} = m_{1.0}\frac{B}{1+B} \tag{10}$$

$$T_{1.2} = T_{1.1} = T_2 = T_{1.0} \tag{11}$$

$$P_{1.2} = P_{1.1} = P_2 = P_{1.0} \tag{12}$$

(3) LPC and HPC

Both the LPC and HPC are compression components. Similar to the FAN, their inlet and outlet parameters satisfy the following constraint equations:

$$m_3 = m_2 = \frac{m_{1.0}}{B+1} \tag{13}$$

$$\varepsilon_{\text{LPC}} = T_3 - T_2 = T_2\left(\pi_{\text{LPC}}^{\frac{k-1}{k}} - 1\right) \Big/ \eta_{\text{C,s}} \tag{14}$$

$$W_{\text{LPC}} = G_2(T_3 - T_2) \tag{15}$$

$$P_3 = \pi_{\text{LPC}} P_2 \tag{16}$$

$$m_5 = m_4 \tag{17}$$

$$\varepsilon_{\mathrm{HPC}} = T_5 - T_4 = T_4\left(\pi_{\mathrm{HPC}}^{\frac{k-1}{k}} - 1\right) \Big/ \eta_{\mathrm{C,s}} \tag{18}$$

$$W_{\mathrm{HPC}} = G_4(T_5 - T_4) \tag{19}$$

$$P_5 = \pi_{\mathrm{HPC}} P_4 \tag{20}$$

(4) CC

In the CC, the air involved in combustion originates from the outlet of the HPC. This portion of air first absorbs waste heat from the exhaust gases through the HEX-4 before entering the CC for combustion. Since part of the high-pressure compressor's final-stage bleed air is used for turbine cooling, the mass flow rate of the air involved in combustion is expressed by the following equation:

$$m_{5.3} = m_5(1 - \delta_{\mathrm{HPC}}) \tag{21}$$

where δ_{HPC} is the compressor bleed air ratio. The hydrogen fuel mass flow rate is $m_{6.1}$, and the mass flow rate of the exhaust gas at the CC outlet is:

$$m_7 = m_{5.3} + m_{6.1} \tag{22}$$

On the basis of the CC pressure recovery factor (σ_{CC}), the outlet gas pressure of the CC can be calculated using the following formula:

$$P_7 = P_{5.3}\sigma_{CC} \tag{23}$$

The thermal-motive force for the combustion process can be calculated using the following equation:

$$\varepsilon_{\mathrm{CC}} = T_7 - T_{5.3} = \frac{m_{6.1} LHV \eta_{CC} + m_{5.3} c_{p,5.3} T_{5.3}}{m_7 c_{p,7}} - T_{5.3} \tag{24}$$

where c_p is the isobaric specific heat capacity, η_{CC} is the combustion efficiency.

The thermophysical properties of the exhaust gas are determined by its composition, which varies with different air and hydrogen fuel mixing ratios. To facilitate the analysis of hydrogen turbofan engine characteristics under varying conditions, the air-to-fuel ratio (AFR) is defined as shown in Eq. (25).

$$AFR = \frac{m_{\mathrm{air}}}{m_{\mathrm{fuel}}} \tag{25}$$

The ambient air is assumed to be humid, with a composition of 77.48 % N_2, 20.59 % O_2, 0.03 % CO_2, and 1.9 % H_2O [20]. The hydrogen combustion equation can be expressed as the following equation.

$$\mathrm{H_2} + AFR\frac{M_{H_2}}{M_{air}}\begin{bmatrix} 0.7748\mathrm{N_2} \\ 0.2059\mathrm{O_2} \\ 0.0003\mathrm{CO_2} \\ 0.019\mathrm{H_2O} \end{bmatrix} \rightarrow \begin{bmatrix} 0.7748AFR\frac{M_{H_2}}{M_{air}}\mathrm{N_2} \\ \left(0.2059AFR\frac{M_{H_2}}{M_{air}} - 0.5\right)\mathrm{O_2} \\ 0.0003AFR\frac{M_{H_2}}{M_{air}}\mathrm{CO_2} \\ \left(0.019AFR\frac{M_{H_2}}{M_{air}} + 1\right)\mathrm{H_2O} \end{bmatrix} \tag{26}$$

where M_{air} is the molar mass of air, taken as 28.757 g/mol, and M_{H2} is the molar mass of hydrogen, taken as 2 g/mol. Based on Eq. (26), the mass ratios of the exhaust gas components can be determined, enabling the calculation of the thermophysical properties and the specific heat ratio of the exhaust gas (k_g).

(5) HPT and LPT

Both the HPT and LPT are expansion components, where the exhaust gas expands and performs work. The mechanical power extracted by these turbines is transmitted through their respective shafts to drive the compressors: the HPT drives the HPC, while the LPT drives the FAN and LPC. In the HPT, two streams of gas participate in the work process: one is the high-temperature gas exhausted from the CC, and the other is the turbine cooling air, which mixes with the main exhaust gas after cooling the turbine to perform work together. Therefore, the HPT is described by the following governing equations:

$$m_8 = m_7 + m_{5.4} \tag{27}$$

$$\varepsilon_{\mathrm{HPT}} = T_7 - T_8 = W_{\mathrm{gas}}/G_7 \tag{28}$$

$$\varepsilon_{54} = T_8 - T_{5.4} = W_{\mathrm{CA}}/G_{5.4} \tag{29}$$

$$W_{\mathrm{HPT}} = W_{\mathrm{gas}} + W_{\mathrm{CA}} \tag{30}$$

$$W_{\mathrm{HPC}} = W_{\mathrm{HPT}}\eta_{\mathrm{m}} \tag{31}$$

$$P_8 = P_7\left[1 - \left(1 - \frac{T_8}{T_7}\right) \Big/ \eta_{\mathrm{T,s}}\right]^{\frac{k_{\mathrm{g,HPT}}}{k_{\mathrm{g,HPT}}-1}} \tag{32}$$

where W_{gas} is the work done by the high-temperature gas, W_{CA} is the work done by the turbine cooling air, $k_{\mathrm{g,HPT}}$ is the specific heat ratio of the exhaust gas flowing through the HPT, and η_{m} and $\eta_{\mathrm{T,s}}$ are the shaft mechanical efficiency and turbine isentropic efficiency, respectively, with their values listed in Table 1.

For LPT, the governing equations are as follows:

$$m_9 = m_8 \tag{33}$$

$$\varepsilon_{\mathrm{LPT}} = T_8 - T_9 = W_{\mathrm{LPT}}/G_8 \tag{34}$$

$$W_{\mathrm{FAN}} + W_{\mathrm{LPC}} = W_{\mathrm{LPT}}\eta_{\mathrm{m}} \tag{35}$$

$$P_9 = P_8\left[1 - \left(1 - \frac{T_9}{T_8}\right) \Big/ \eta_{\mathrm{T,s}}\right]^{\frac{k_{\mathrm{g,LPT}}}{k_{\mathrm{g,LPT}}-1}} \tag{36}$$

where $k_{\mathrm{g,LPT}}$ is the specific heat ratio of the exhaust gas flowing through the LPT.

(6) HEX-4 (Recuperator)

A small portion of the high-pressure, high-temperature air exiting the HPC serves as turbine cooling air, while the remaining portion flows into HEX-4 to recover waste heat from the turbine exhaust gas. Both streams exit the HPC at the same temperature and pressure. Based on the global heat current network model illustrated in Fig. 3, applying Kirchhoff's voltage law yields the constraint equations satisfied by HEX-4.

$$T_{5.1} = T_{5.2} = T_5 \tag{37}$$

$$m_{10} = m_9 \tag{38}$$

$$m_{5.1} = m_{5.3} \tag{39}$$

$$T_9 - T_{5.1} = Q_4 R_4 \tag{40}$$

$$\varepsilon_{51,53} = T_{5.3} - T_{5.1} = Q_4/G_{5.1} \tag{41}$$

$$\varepsilon_{9,10} = T_9 - T_{10} = Q_4/G_9 \tag{42}$$

$$R_4 = \frac{G_{5.1}\exp\left(\frac{KA_4}{G_9}\right) - G_9\exp\left(\frac{KA_4}{G_{5.1}}\right)}{G_9 G_{5.1}\left[\exp\left(\frac{KA_4}{G_9}\right) - \exp\left(\frac{KA_4}{G_{5.1}}\right)\right]} \tag{43}$$

$$P_{10} = P_9\sigma_{\mathrm{HEX}} \tag{44}$$

where R_4 is the inlet temperature difference-based thermal resistance of HEX-4, KA_4 is the thermal conductivity of HEX-4, σ_{HEX} is the HEX pressure recovery factor listed in Table 1.

(7) EDN

Considering the expansion ratio of the EDN is relatively small and can be neglected, the inlet and outlet parameters satisfy the following relationship:

$$m_{11} = m_{10} \tag{45}$$

$$T_{11} = T_{10} \tag{46}$$

$$P_{11} = P_{10} \tag{47}$$

(8) Intermediate cycle heat exchange system

For the intermediate cycle heat exchange system, applying the heat current method can effectively reduce unknown intermediate variables [45], simplify the governing equations, and facilitate solutions. By combining the heat current model of the synergistic heat recovery-dissipation architecture for hydrogen turbofan engines shown in Fig. 3 and replacing the thermos-motive forces with their definitions, the resulting constraint equations are:

$$T_3 - T_4 = Q_1/G_3 \tag{48}$$

$$T_3 - T_{12} = Q_1 R_1 - (Q_1 + Q_2)/G_{He} \tag{49}$$

$$T_{5.2} - T_{12} = Q_2 R_2 - (Q_1 + Q_2)/G_{He} \tag{50}$$

$$T_{5.2} - T_{5.4} = Q_2/G_{5.2} \tag{51}$$

$$Q_3 = Q_1 + Q_2 \tag{52}$$

$$G_{He} = G_{He,1} + G_{He,2} \tag{53}$$

$$P_4 = P_3 \sigma_{HEX} \tag{54}$$

$$P_{5.4} = P_{5.2}\sigma_{HEX} = P_5 \sigma_{HEX} \tag{55}$$

where Q_i denotes the heat transfer rate of HEX$_i$, G_{He}, $G_{He,1}$, and $G_{He,2}$ represent the heat capacity flow rates of helium through HEX-3, HEX-1, and HEX-2, respectively. R_1 and R_2 denote the thermal resistance of HEX-1 and HEX-2, respectively, with their calculation expressions as follows:

$$R_1 = \frac{G_{He,1}\exp\left(\frac{KA_1}{G_3}\right) - G_3\exp\left(\frac{KA_1}{G_{He,1}}\right)}{G_{He,1}G_3\left[\exp\left(\frac{KA_1}{G_3}\right) - \exp\left(\frac{KA_1}{G_{He,1}}\right)\right]} \tag{56}$$

$$R_2 = \frac{G_{He,2}\exp\left(\frac{KA_2}{G_{5.2}}\right) - G_{5.2}\exp\left(\frac{KA_2}{G_{He,2}}\right)}{G_{He,2}G_{5.2}\left[\exp\left(\frac{KA_2}{G_{5.2}}\right) - \exp\left(\frac{KA_2}{G_{He,2}}\right)\right]} \tag{57}$$

$$G_{He} = m_{12}c_{p,12} \tag{58}$$

$$G_{He,1} = (m_{12}\phi)c_{p,13.1} \tag{59}$$

$$G_{He,1} = m_{12}(1-\phi)c_{p,13.2} \tag{60}$$

where ϕ is the distribution ratio of helium flow in branches (defined in Eq. (61)) with the value listed in Table 1.

$$\phi = m_{13.1}/m_{12} = 1 - m_{13.2}/m_{12} \tag{61}$$

The equations above represent two independent branches within the heat current model, forming linear combinations of thermal resistances, heat transfer rates, and thermo-motive forces. Moreover, the system's nonlinearity is fully embedded in the expressions for thermal resistances. However, since LH_2 undergoes a phase change in HEX-3, causing significant variations in its thermal properties, the thermal resistance definition in Eq. (1) becomes inapplicable. Therefore, a phase-change-coupled LH_2 preheating model needs to be developed to extend the applicability of the heat current method to hydrogen-fueled engines. This will be discussed in Section 3.3.

3.3. Phase-change coupled LH_2 preheating modeling

For hydrogen-fueled aero engines, hydrogen is stored in liquid form; however, most existing studies have not considered the utilization of LH_2 heat sink, and engine thermal modeling that incorporates a LH_2 preheating model with phase-change coupling remains very limited. Instead, prior works [21–24] have primarily focused on the changes in thermodynamic performance and economic efficiency arising from substituting hydrogen for conventional aviation fuels. To address this gap, the present study further develops a phase-change coupled LH_2 preheating model.

LH_2 undergoes a phase change in HEX-3, resulting in significant variations in its thermal properties. To ensure the accuracy of the hydrogen-fueled engine thermodynamic model, the global heat current network must be coupled with the LH_2 phase change model. Fig. 4 illustrates the phase-change coupled LH_2 preheating model, which adopts a multi-stage segmentation approach. The LH_2 from the storage tank is in a saturated state at the saturation temperature ($T_{saturation}$). Therefore, the LH_2 preheater is divided into two zones: the evaporation zone and the superheating zone. In the evaporation zone, the hydrogen temperature remains constant at $T_{saturation}$, and the heat exchanged with helium corresponds to the latent heat of vaporization of LH_2 is Q_{evapor}. Defining the inlet temperature of helium entering the evaporation zone as T_{sup}, the following relationship holds in the evaporation zone:

$$Q_{evapor} = m_{hydrogen}L_v \tag{62}$$

$$h|_{T_{sup}} = Q_{evapor}\Big/m_{helium} + h|_{T_{h,out}} \tag{63}$$

where L_v represents the latent heat of vaporization of hydrogen, obtained from the CoolProp library [56], and h represents the specific enthalpy of helium.

In the superheating zone, hydrogen remains in a single phase (gaseous), but its thermal properties continue to change significantly. Therefore, it is divided into n segments, each with an equal amount of heat transfer rate (ΔQ), as shown in Fig. 4. The energy flow topology is applied step-by-step to each segment of the hydrogen preheater. Fig. 5 illustrates the equivalent energy flow model within HEX-3, representing the heat flow transfer across each segment. Based on Figs. 4 and 5 and applying Kirchhoff's voltage law, the following constraint equations are obtained:

$$Q_3 = Q_{sup} + Q_{evapor} \tag{64}$$

$$n = Q_{sup}/\Delta Q \tag{65}$$

$$R_3(i) = \frac{G_{H_2}(i)\exp\left(\frac{KA_3}{G_{He}}\right) - G_{He}\exp\left(\frac{KA_3}{G_{H_2}(i)}\right)}{G_{H_2}(i)G_{He}\left[\exp\left(\frac{KA_3}{G_{He}}\right) - \exp\left(\frac{KA_3}{G_{H_2}(i)}\right)\right]} \tag{66}$$

$$T_{h,in}(i) = T_{c,in}(i) + \Delta Q R_3(i) \tag{67}$$

$$T_{c,out}(i) = T_{c,in}(i) + \Delta Q/G_{H_2}(i) \tag{68}$$

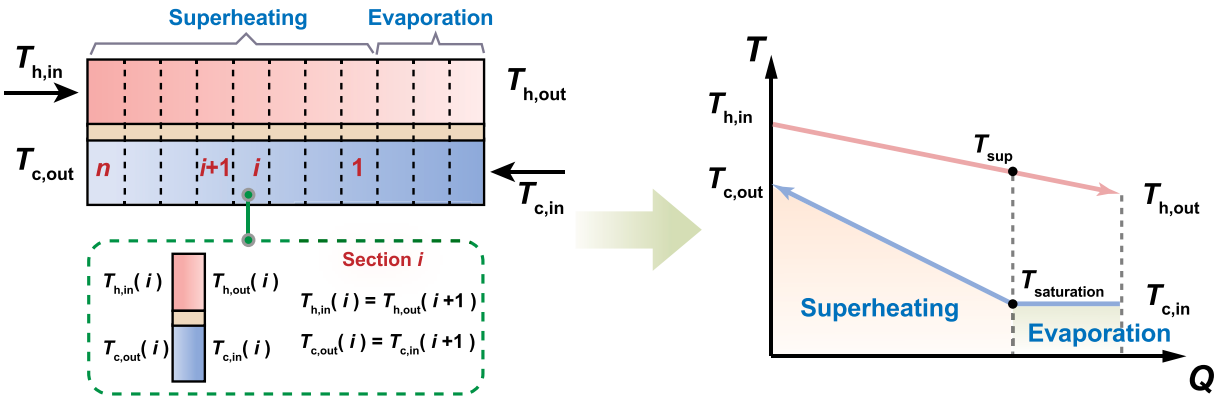

Fig. 4. Schematic diagram of the phase-change coupled LH_2 preheating model.

$$T_{h,out}(i) = T_{h,in}(i) - \Delta Q / G_{He} \tag{69}$$

$$\begin{cases} T_{h,in}(n) = T_{12} \\ T_{h,out}(1) = T_{sup} \\ T_{c,in}(1) = T_6 = T_{saturation} \\ T_{c,out}(n) = T_{6.1} \end{cases} \tag{70}$$

where Q_{sup} is the heat transfer rate in the superheating zone, ΔQ is the heat transfer rate in each segment, set to 1 kW, n is the number of segments, i represents the i-th segment, and G_{H2} is the heat capacity flow rate of hydrogen in the i-th segment.

3.4. Solution strategy and model validation

Based on the aforementioned global heat current model, the calculation procedure of the proposed synergistic heat recovery-dissipation architecture for hydrogen turbofan engines is depicted in Fig. 6. Fig. 6 consists of four main modules: parameters input (engine, HEXs, and flight conditions), component-level modeling, phase-change coupled LH_2 preheating modeling, and performance evaluation. First, the parameters are input; then, component-level modeling is performed based on Section 3.2 (Eqs. (2)-(61)). Within this modeling, HEX-3 requires the phase-change coupled LH_2 preheating model described in Section 3.3 (Eqs. (62)-(70)). Subsequently, the engine governing equations derived from the above modeling are solved iteratively, and finally, performance evaluation is carried out based on the obtained thermodynamic parameters. Engine parameters for simulation are given in Table 1 in detail, and the thermal conductivity for different HEX is listed in Table 2. According to Ref. [57], the storage pressure of LH_2 is set at 0.5 MPa, corresponding to the inlet pressure P_6 of LH_2 in HEX-3. In the specific solution process, the number of unknown variables matches the number of constraint equations, ensuring a unique solution for the system. On the basis of the thermodynamic parameters of each component of the hydrogen turbofan engine obtained from the solution, the engine's thermodynamic performance, thrust, and economic efficiency can be evaluated. Additionally, the engine parameters listed in Table 1 can be adjusted to analyze the effect of different parameters on the performance of the hydrogen turbofan engine.

To validate the hydrogen engine heat current model established in Sections 3.1–3.2, the modeling method developed in this study is applied to recalculate the thermodynamic parameters of the hydrogen-modified TF33 turbofan engine from Ref. [20]. It should be noted that Ref. [20] did not consider the preheating process of LH_2 but instead directly supplied hydrogen gas at 298.15 K to the CC. Therefore, the phase-change coupled LH_2 preheating model proposed in Section 3.3 is not validated in the comparative calculations with the reference. However, the computational analysis presented in Chapter 4 demonstrates that the calculated heat transfer rate Q_3 for the hydrogen preheater matches the enthalpy difference corresponding to the modeled outlet

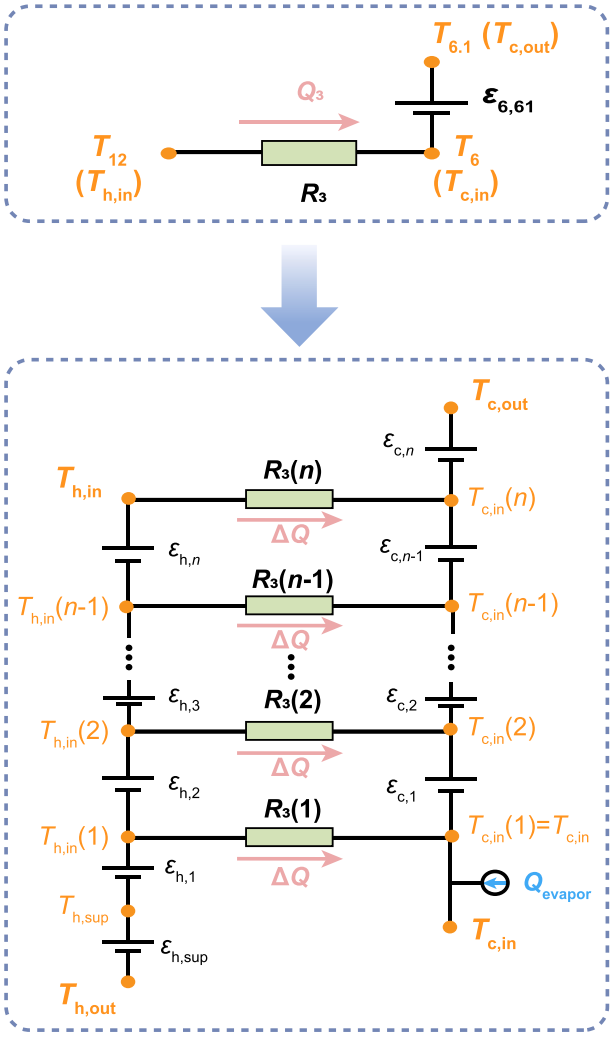

Fig. 5. The internal equivalent energy flow model for hydrogen preheater.

and inlet temperatures of hydrogen, thereby confirming the reliability of the phase-change coupled LH_2 preheating model.

Table 3 compares the simulation results of this study with the data from Ref. [20], where the station numbers correspond to those defined in the reference. It can be observed that the maximum temperature prediction deviation is 23.15 K, corresponding to the LPT outlet, while the maximum pressure prediction deviation is −10.72 %, corresponding to the HPT outlet. For all nodes upstream of the HPT inlet, the prediction deviation is less than 1 %. Fig. 7(a) compares the temperature and

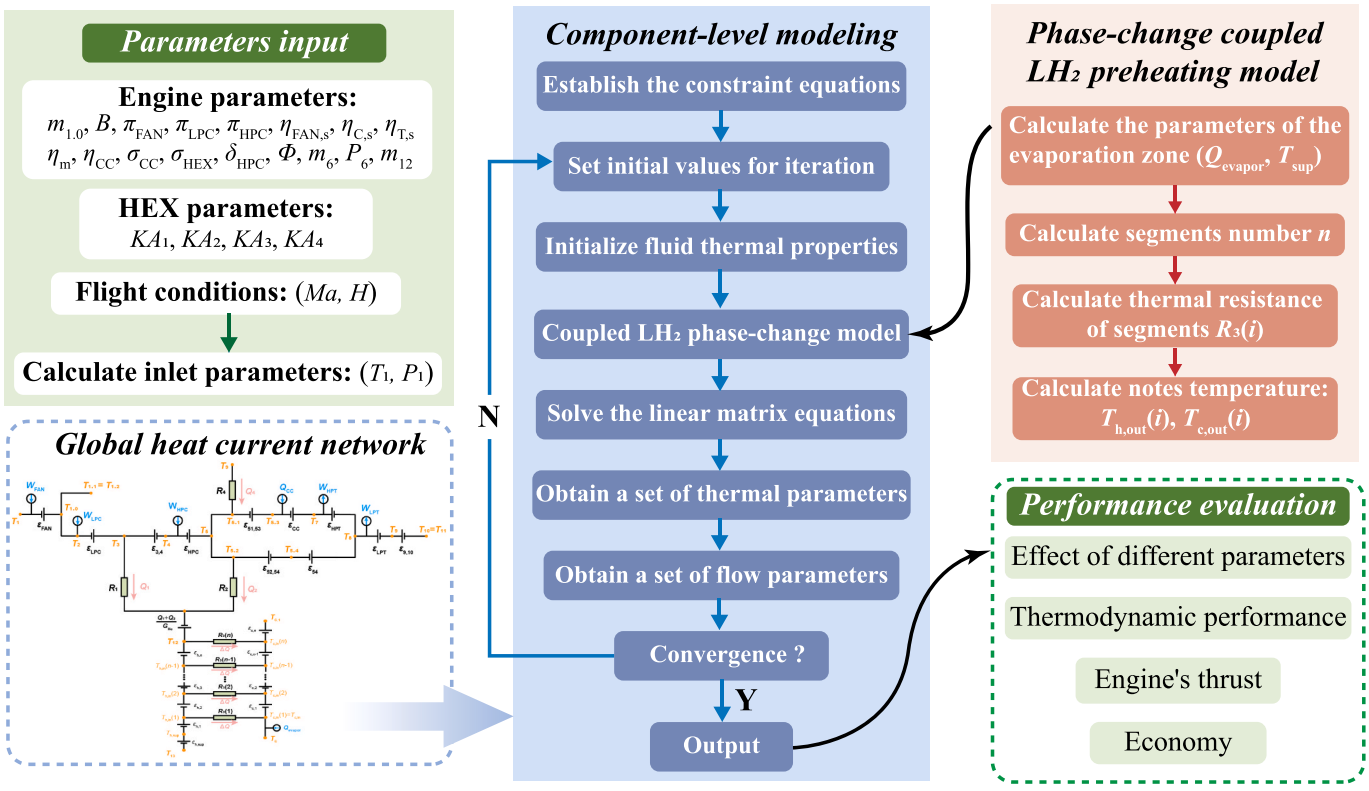

Fig. 6. Calculation flowchart of the global heat current model of the synergistic heat recovery-dissipation architecture for hydrogen turbofan engines.

Table 2
The thermal conductivity for different HEX.

KA_1 (kW/K)	KA_2 (kW/K)	KA_3 (kW/K)	KA_4 (kW/K)
6	2	10	3

pressure variations across each engine component between this study and the reference. In terms of absolute values, the maximum pressure deviation is 54.8 kPa, which is relatively small. Fig. 7(b) illustrates the prediction error distribution for all calculated data points. The larger prediction errors are concentrated in the turbine region because the reference did not account for variations in the thermal properties of the exhaust gas or changes in the specific heat ratio (k_g) with temperature and pressure. In contrast, the model developed in this study iteratively updates the thermal properties of each working fluid based on temperature and pressure during the simulation process. Overall, the small prediction errors demonstrate the high accuracy of the modeling method used in this study.

4. Results and discussion

This section analyzes the influence of key thermodynamic parameters on the performance of the proposed hydrogen turbofan engine. The independent variables—bypass ratio (B), turbine inlet temperature (T_7), helium mass flow rate (m_{12}), and distribution ratio of helium flow in branches (ϕ)—along with their reference values and variation ranges, are listed in Table 4. All results and discussions are carried out under standard sea-level-static conditions. The thermodynamic analysis indicators associated with aero-engine performance are systematically categorized in Table 5.

4.1. Effect of the bypass ratio

The effect of bypass ratio B on HEX performance is clearly illustrated in Fig. 8. Fig. 8(a) presents the variations in temperature drop or rise on the air side of the HEXs within the system as a function of bypass ratio. As the bypass ratio increases, the temperature difference between the inlet and outlet on the air side of each HEX increases monotonically,

Table 3
Comparison of simulation results of the present model with reference.

Station No.	Fluid type	Ref. T (K)	Cal. T (K)	Error of T (K)	Ref. P (kPa)	Cal. P (kPa)	Error of P (%)
1	Air	288.15	288.15	0.00	101.33	101.33	0.00
2	Air	350.40	350.32	0.08	179.21	179.20	0.01
3	Air	350.40	350.32	0.08	179.21	179.20	0.01
4	Air	348.65	350.32	1.67	177.42	179.20	−1.00
5	Air	350.40	350.32	0.08	179.21	179.20	0.01
6	Air	461.37	461.09	0.28	434.25	434.23	0.00
7	Air	652.60	652.90	0.30	1378.57	1378.50	0.01
8	Fuel	298.15	298.15	0.00	220.60	220.60	0.00
9	Exhaust gas	1098.42	1108.77	10.35	1309.60	1309.57	0.00
10	Exhaust gas	942.82	944.01	1.19	510.50	565.25	−10.72
11	Exhaust gas	743.23	720.08	23.15	135.45	140.04	−3.39
12	Exhaust gas	740.07	720.08	19.99	133.25	140.04	−5.10

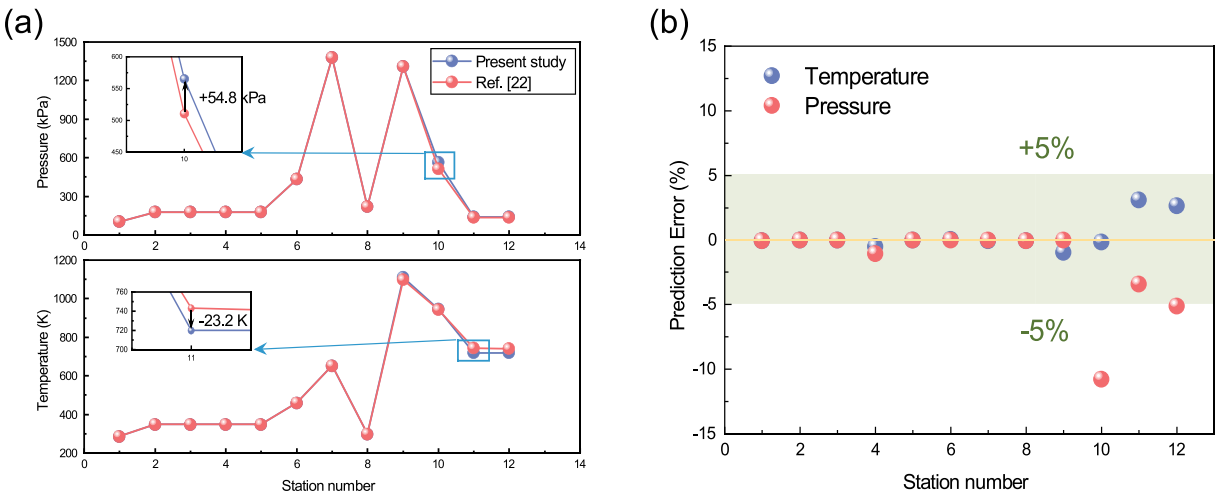

Fig. 7. Heat current model validation. (a) Comparison of temperature and pressure variations of the flow through the components; (b) prediction errors of all data.

Table 4
The reference value and variation range of the independent variables.

Independent variables	Unit	Reference value	Variation range
Bypass ratio, B	/	1.2	2.2–3.6
Turbine inlet Temperature, T_7	K	1800	1500–2200
Helium mass flow rate, m_{12}	kg/s	1	0.2–1.8
Distribution ratio of helium flow in branches, ϕ	/	0.8	0.1–0.9

exhibiting a near-linear trend. Among them, the variation in HEX-2 is the most pronounced, with the air-side temperature drop reaching up to 167.9 K. This behavior arises because a higher bypass ratio corresponds to a reduction in core airflow, while the system's cold source remains unchanged. Consequently, for HEX-1 and HEX-2, the diminished heat source results in a greater air-side temperature drop. In the case of the recuperator HEX-4, although the reduction in core airflow leads to a lower exhaust gas mass flow rate (m_9), the turbine inlet temperature increases significantly (as shown in Fig. 9(b)), thereby elevating the hot-side inlet temperature of HEX-4. Considering the combined effects of mass flow rate and temperature, the air-side temperature rise across HEX-4 also increases with the bypass ratio. The variations in heat transfer rate for each HEX are presented in Fig. 8(b). Based on the above analysis, for the intermediate cycle heat exchange system, the reduction in system heat sources leads to a monotonic decrease in the heat transfer rates of the internal HEXs (Q_1–Q_3). In contrast, the heat transfer rate of HEX-4 (Q_4) increases significantly due to the enlarged temperature difference across the exchanger. Notably, when the bypass ratio exceeds 2.4, Q_4 surpasses Q_3. It is worth noting that Q_3 represents the heat transfer capacity of the intermediate cycle heat exchange system, which is theoretically equal to the sum of Q_1 and Q_2.

The variation in compressor power consumption with bypass ratio is illustrated in Fig. 9(a). Since the airflow is divided into the bypass and core ducts only after passing through the fan, the fan power consumption (W_{FAN}) remains unaffected by changes in bypass ratio and remains constant at 8297.9 kW. As both the LPC and HPC are located in the core duct, the volume of air they compress decreases with increasing bypass ratio, resulting in a corresponding reduction in their power consumption. Furthermore, Fig. 9(a) shows that the power consumption of the HPC consistently exceeds that of the LPC by a factor of approximately 2.5. As depicted in Fig. 9(b), the turbine inlet temperature (T_7) increases monotonically with the bypass ratio, which can be explained by Eq. (24). Based on current turbine cooling technology, where the maximum allowable turbine inlet temperature is approximately 2200 K [53], the upper limit for the bypass ratio in the proposed hydrogen turbofan engine is determined to be 2.33. The preheated hydrogen temperature ($T_{6.1}$), which also corresponds to the hydrogen inlet temperature to the CC, decreases with increasing bypass ratio and exhibits a linear trend.

Fig. 10 presents the variation of key performance parameters of the aviation engine with bypass ratio, including thrust ratio, thermal efficiency, specific thrust, thrust, specific fuel consumption, and specific fuel cost rate. As the bypass ratio increases, the thrust ratio rises

Table 5
General thermodynamic indicators related to aero engines.

Thermodynamic indicators	Definitions	Calculation equations
Thrust, F	The force generated by the engine to propel the aircraft forward.	$F = m_{11}V_{EDN} + m_{1.2}V_{FDN} - m_1V_1$
Specific thrust, F_s	Thrust produced per unit mass flow rate of air through the engine; indicates the engine's propulsion efficiency.	$F_s = F/m_1$
Thermal efficiency, η_{th}	The ratio of the net work output to the thermal energy input from fuel; reflects how effectively the engine converts fuel energy into mechanical energy.	$\eta_{th} = \frac{(m_{11}V_{EDN}^2 + m_{1.2}V_{FDN}^2 - m_1V_1^2)/2}{m_6LHV \times 1000}$
Specific fuel consumption, SFC	The fuel mass flow rate required to produce a unit of thrust; an indicator of engine fuel efficiency.	$SFC = \frac{3600m_6}{F}$
Fuel cost rate, FCR	The monetary cost of fuel consumed per unit time. H_2 selling price is 4.94 $/kg [58].	$FCR = 4.94m_6$
Specific fuel cost rate, $SFCR$	The ratio of fuel cost rate to engine thrust; quantifies the economic cost of fuel per unit of thrust, typically expressed in $/(kN·s).	$SFCR = \frac{FCR}{F}$
Thrust ratio	The ratio of fan thrust (F_{FAN}) to core thrust (F_{core}); reflects the relative contribution of bypass (fan) flow versus core flow in generating total engine thrust.	Thrust ratio $= F_{FAN}/F_{core}$

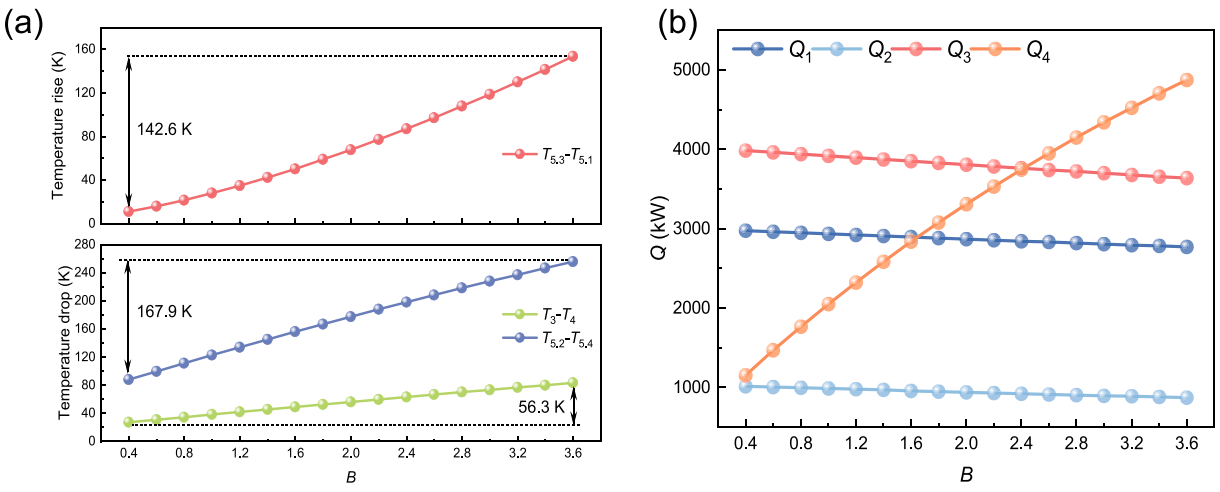

Fig. 8. Effect of bypass ratio on (a) temperature drop or rise on the air side of the HEXs within the system; (b) heat transfer rate of different HEX.

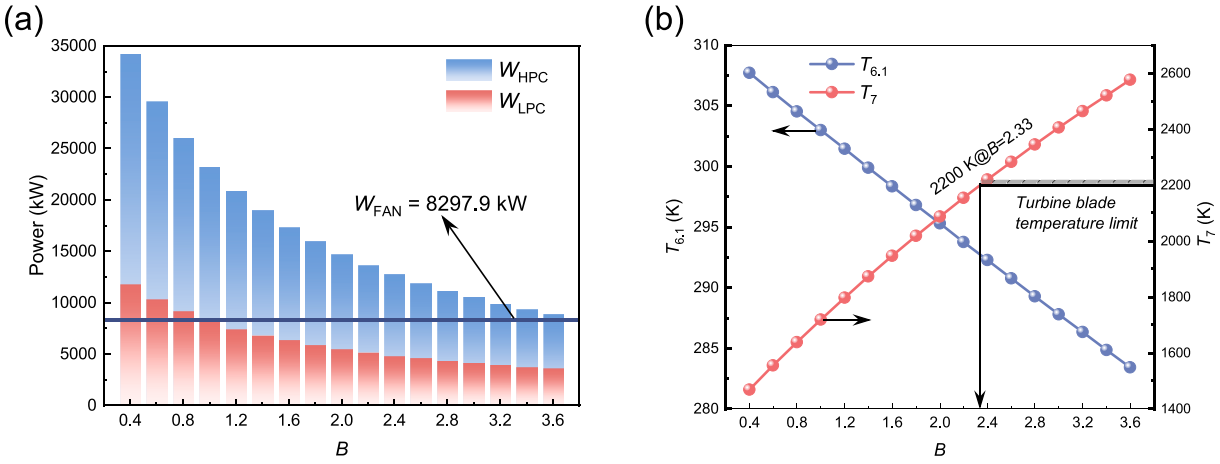

Fig. 9. Effect of bypass ratio on (a) compressor power consumption; (b) turbine inlet temperature T_7 and preheated hydrogen temperature $T_{6.1}$.

monotonically, indicating that the fan's contribution to total engine thrust becomes increasingly dominant. The thermal efficiency initially increases rapidly and then gradually declines, reaching a maximum value of $\eta_{th} = 0.507$ at $B = 2.4$. Besides, both the engine thrust (F) and specific thrust (F_s) decrease with increasing bypass ratio. The optimum B that maximizes η_{th} follows directly from the definition of η_{th}. With $m_6 LHV$ fixed, the optimum arises from how the net jet kinetic energy in the numerator varies with B. As B increases, the core mass flow rate m_{11} decreases and the core jet speed V_{EDN} tends to drop, whereas the bypass mass flow rate $m_{1.2}$ increases and the bypass jet speed V_{FDN} tends to rise. In addition, changes in heat exchange modify thermal properties and therefore both jet velocities. These two kinetic-energy contributions thus move in opposite directions with B, and the thermal efficiency peaks at the point $B = 2.4$. Fig. 10(b) illustrates the trends in specific fuel

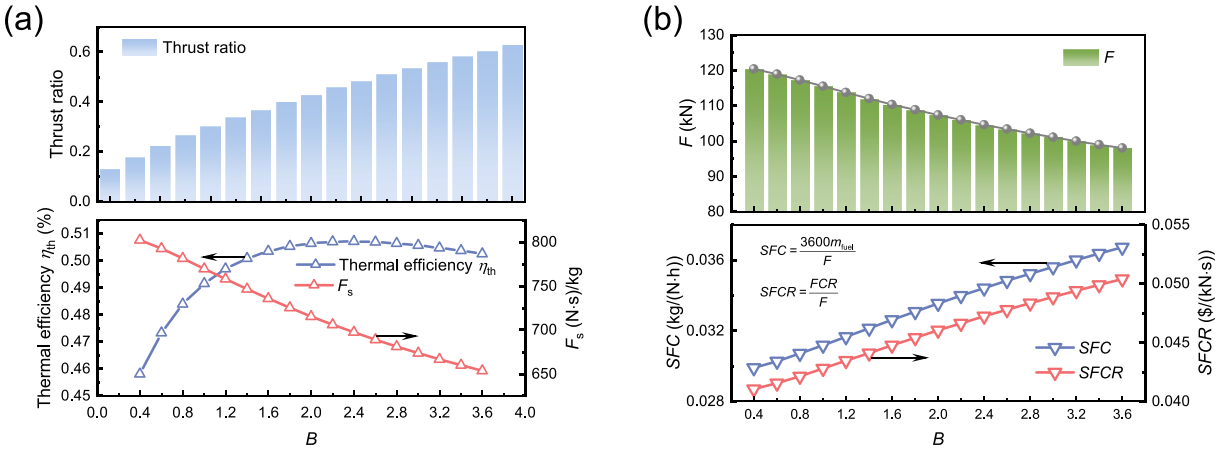

Fig. 10. Effect of bypass ratio on (a) Thermal efficiency, specific thrust, and thrust ratio; (b) specific fuel consumption, specific fuel cost rate, and engine thrust.

consumption (*SFC*) and specific fuel cost rate (*SFCR*) with increasing bypass ratio. Both *SFC* and *SFCR* increase nearly linearly, indicating that a higher bypass ratio results in greater fuel consumption per unit thrust, thereby reducing propulsive efficiency. Additionally, the economic cost of fuel per unit thrust also rises. Since hydrogen is generally more expensive than aviation kerosene, the increase in *SFCR* directly translates into less favourable economic performance. These trends suggest that a higher design bypass ratio may adversely affect the economic performance of the hydrogen turbofan engine. Additionally, based on the calculation equations in Table 5, it can be readily derived that when the fuel mass flow rate (m_{fuel} or m_6) remains constant, both *SFC* and *SFCR* are linear functions of F^{-1}, which explains their identical trends.

4.2. Effect of the turbine inlet temperature

The turbine inlet temperature (T_7) directly influences both the thermal efficiency and propulsive power of aviation engines, making it a critical parameter in evaluating the thermodynamic performance of the hydrogen turbofan engine. According to Eq. (24), T_7 is directly correlated with the hydrogen mass flow rate. Therefore, in the analysis presented in this section, variations in T_7 effectively reflect changes in the hydrogen mass flow rate (m_6). Fig. 11 illustrates the variation of fuel mass flow rate and preheated hydrogen temperature ($T_{6.1}$) with T_7. As shown in Fig. 11, an increase in T_7, corresponding to a higher m_6, indicates an enhancement of the system's cold source. As a result, $T_{6.1}$ decreases accordingly. It is important to note that excessively low hydrogen temperatures may hinder ignition and compromise stable combustion within the CC. Fig. 12(a) depicts the variations in temperature drop or rise on the air side of the HEXs within the system as a function of T_7. With elevated values of T_7, a near-linear enhancement in the air-side temperature difference is observed across the HEXs. HEX-2 demonstrates the highest sensitivity to this parameter change, marked by a maximum reduction of 48.6 K. Fig. 12(b) illustrates the changes in heat transfer rate across each HEX (Q_1–Q_4), all of which exhibit an increasing trend. These phenomena can be explained as follows: in the intermediate cycle heat exchange system, an increase in m_6 signifies an enhancement of the available LH_2 heat sink, which in turn increases the temperature difference between the inlet and outlet on the air side of HEXs and elevates the corresponding heat transfer rates. For the recuperator HEX-4, the rise in T_7 leads to a higher inlet temperature of the hot-side exhaust gas. Simultaneously, the presence of the intercooler HEX-1 lowers the inlet temperature of the cold-side air. The combined effect of these two factors enlarges the temperature difference across HEX-4, resulting in an increased heat transfer rate Q_4. Since the air mass flow rate $m_{5.1}$ remains constant, the air-side temperature rise ($T_{5.3}$-$T_{5.1}$) increases accordingly.

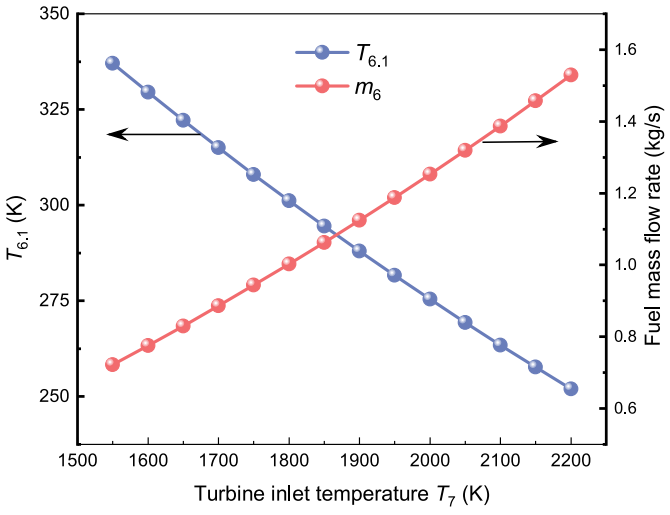

Fig. 11. Effect of turbine inlet temperature T_7 on fuel mass flow rate m_6 and preheated hydrogen temperature $T_{6.1}$.

The impact of T_7 on key engine performance metrics is depicted in Fig. 13. A higher T_7 leads to a steady decrease in the thrust ratio, suggesting a greater contribution of the core engine to the engine's total thrust. Since the intercooler HEX-2 is positioned downstream of the LPC, variations in T_7 do not affect the power consumption of the FAN or LPC. However, as shown in Fig. 13(a), the power consumption of the HPC (W_{FAN}) decreases with increasing T_7. This reduction results from the synergistic heat recovery–dissipation architecture, which lowers the thermal load on the HPC and consequently reduces the rotor's work requirement. Both F_s and F increase nearly linearly with T_7; as T_7 increases from 1550 K to 2200 K, F_s rises from 648.2 (N s)/kg to 914.3 (N s)/kg. While η_{th} initially increases and then levels off, reaching a maximum value of approximately 0.505.

The influence of T_7 on *SFC* and *SFCR* follows the same trend as that of the bypass ratio—both increase monotonically. These results highlight that performance improvements are not always accompanied by economic benefits. For example, increasing the B or T_7 enhances thermal efficiency and F_s, but it also leads to higher *SFC* and *SFCR*. In practical terms, this means that achieving better propulsive and thermal efficiency requires burning more hydrogen per unit thrust, thereby raising operational fuel costs. Since hydrogen is generally more expensive than conventional kerosene, the increase in *SFC/SFCR* directly translates into less favourable economic performance. This performance–economics trade-off underscores the importance of balancing thermodynamic optimization with fuel cost considerations in future design studies. Unlike the mechanism by which the bypass ratio influences engine performance, both F and m_6 vary with T_7. Fig. 13(b) presents the variation of the normalized parameters $m_6/m_{6,min}$ and F/F_{min} with T_7, showing that the slope of $m_6/m_{6,min}$ is steeper, indicating a faster growth rate of m_6. Therefore, both *SFC* and *SFCR* increase with increasing T_7.

4.3. Effect of the helium mass flow rate

The components within the intermediate cycle heat exchange system are interconnected through the intermediate working fluid—helium. The mass flow rate and distribution ratio of helium directly influence the system's heat transfer characteristics, thereby affecting the overall performance of the hydrogen turbofan engine. Furthermore, under varying flight conditions, appropriately adjusting the helium mass flow rate is essential for optimizing the performance of the intermediate cycle heat exchange system and achieving effective thermal control of the engine [26]. Fig. 14(a) presents the variations in temperature drop or rise on the air side of the HEXs within the system as a function of helium mass flow rate m_{12}. The air-side temperature differences between the inlet and outlet of all HEXs decrease rapidly with increasing m_{12}, and then gradually approach a plateau. However, the impact on the recuperator HEX-4 is relatively limited, with the air-side temperature rise varying by only 3.0 K. The variations in heat transfer rate for each HEX are presented in Fig. 14(b). As m_{12} increases, Q_1–Q_3 exhibit a trend of rapid decline followed by gradual stabilization, while Q_4 is only marginally affected—consistent with the variation observed in the air temperature rise curve ($T_{5.3}$−$T_{5.1}$). This suggests that the regulatory capacity of the intermediate working fluid mass flow rate is limited; once m_{12} exceeds a threshold (approximately 1.4 kg/s), the system becomes increasingly insensitive to further increases. Moreover, an excessively high m_{12} reduces the thermal load within the intermediate cycle heat exchange system, which is detrimental to the deep energy utilization of the engine.

The variation in turbine inlet temperature (T_7) and preheated hydrogen temperature ($T_{6.1}$) with m_{12} is illustrated in Fig. 15(a). The preheated hydrogen temperature $T_{6.1}$ varies significantly with changes in m_{12}; as m_{12} increases from 0.2 kg/s to 1.8 kg/s, $T_{6.1}$ decreases markedly from 461.2 K to 234.2 K. In contrast, T_7 increases with rising m_{12}, but the variation is relatively minor—only 48.9 K. These results

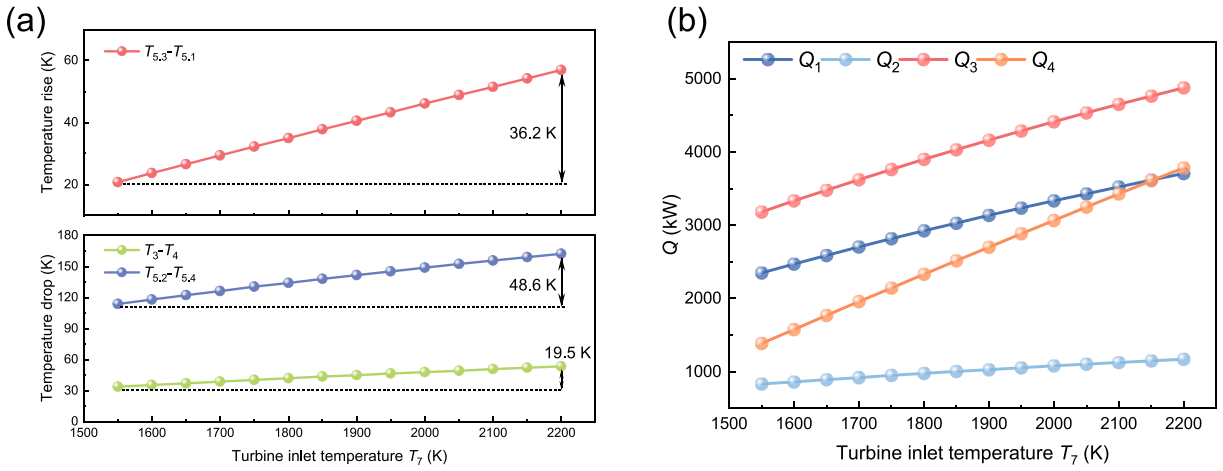

Fig. 12. Effect of turbine inlet temperature T_7 on (a) temperature drop or rise on the air side of the HEXs within the system; (b) heat transfer rate of different HEX.

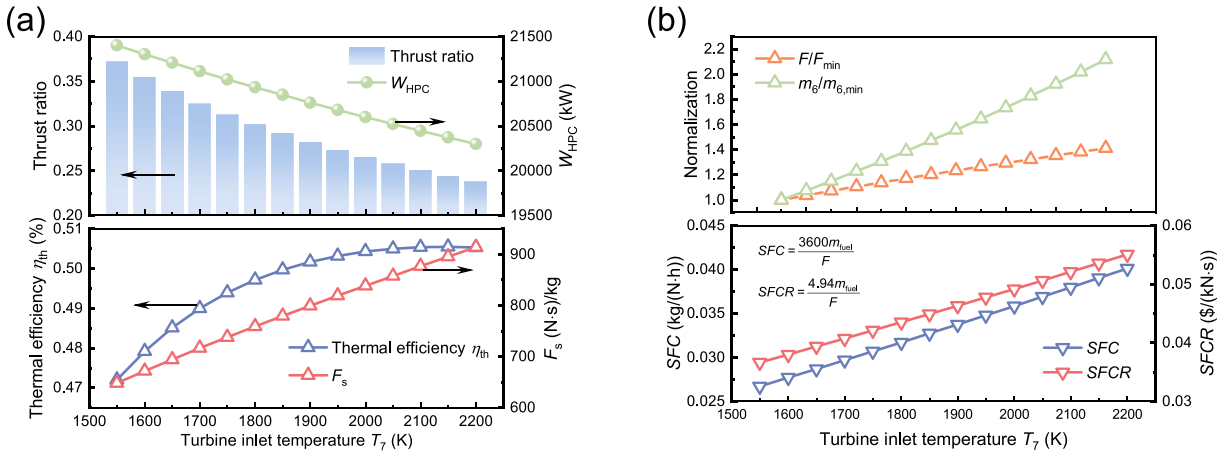

Fig. 13. Effect of bypass ratio on (a) Thermal efficiency, specific thrust, thrust ratio, and HPC power consumption; (b) specific fuel consumption, specific fuel cost rate, and normalization parameters.

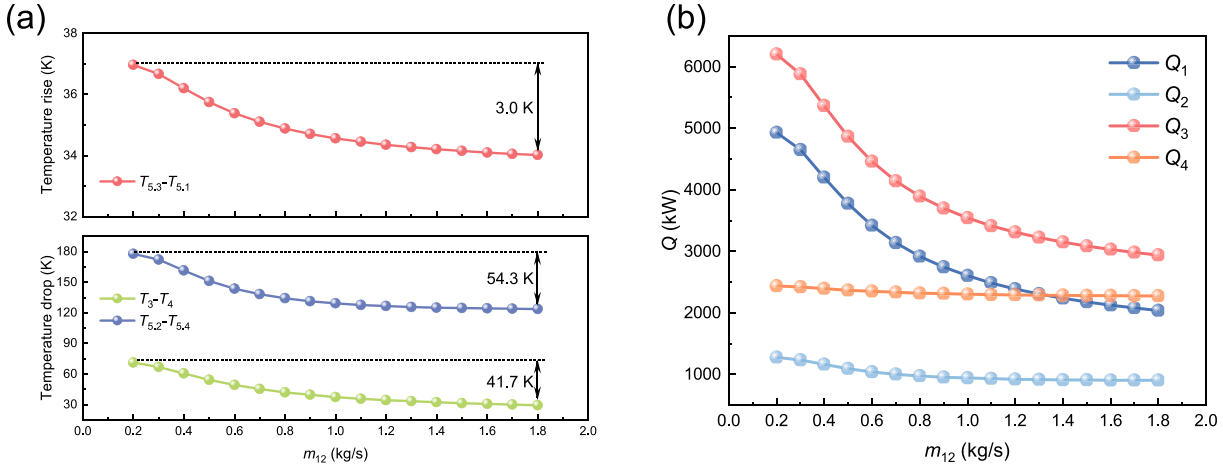

Fig. 14. Effect of helium mass flow rate m_{12} on (a) temperature drop or rise on the air side of the HEXs within the system; (b) heat transfer rate of different HEX.

indicate that m_{12} indirectly influences the engine's actual operating parameters by modulating the heat transfer characteristics of the intermediate cycle heat exchange system. Fig. 15(b) presents the variation of W_{HPC}, F_s, and η_{th} with m_{12}. As observed, both F_s and η_{th} decrease with increasing m_{12}, though the magnitudes of change are relatively small—less than 0.01 for η_{th} and less than 6 (N•s)/kg for F_s. This suggests that the increase in m_{12} has a minor negative impact on engine thrust and efficiency. Additionally, W_{HPC} also exhibits an increasing trend. Based on the above analysis, it can be concluded that a lower intermediate working fluid mass flow rate provides multiple advantages for the

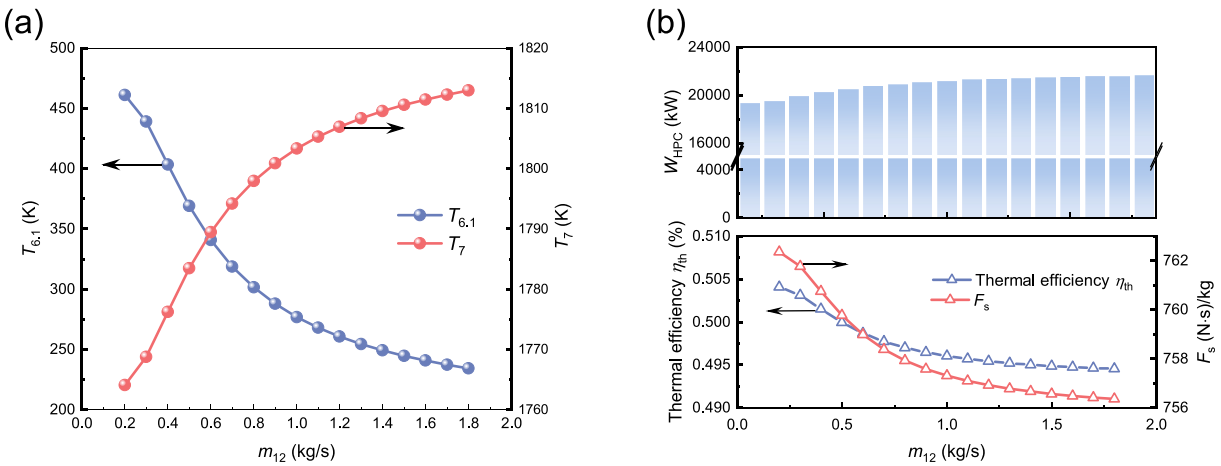

Fig. 15. Effect of helium mass flow rate m_{12} on (a) turbine inlet temperature T_7 and preheated hydrogen temperature $T_{6.1}$; (b) thermal efficiency, specific thrust, and HPC power consumption.

thermodynamic performance of the proposed hydrogen turbofan engine, including more efficient thermal energy utilization, a higher preheated hydrogen temperature—favourable for ignition and stable combustion, and improved F_s and η_{th}.

4.4. *Effect of the distribution ratio of helium flow in branches*

The effect induced by the distribution ratio of helium flow in branches (ϕ) is displayed in Fig. 16. In the simulation, the helium mass flow rate in the main loop of the intermediate cycle heat exchange system (m_{12}) is fixed at 1 kg/s. A larger ϕ indicates a higher helium mass flow rate on the cold side of the intercooler HEX-1 and a correspondingly lower mass flow rate on the cold side of the CCA cooler HEX-2.

Fig. 16(a) depicts the variations in temperature drop or rise on the air side of the HEXs within the system as a function of ϕ. As ϕ increases, the air-side temperature difference across HEX-1 increases monotonically, whereas that across HEX-2 initially rises slowly and then declines rapidly. For HEX-1, an increase in ϕ corresponds to a greater available heat sink on the cold side, leading to a larger air-side temperature difference between the inlet and outlet. In contrast, for HEX-2, although a higher ϕ reduces the available cold-side heat sink, the upstream HEX-1 lowers the air inlet temperature to HEX-2, thereby increasing the heat transfer temperature difference. As a result of these competing effects, the air-side temperature difference across HEX-2 exhibits a non-monotonic dependence on ϕ. Since the recuperator HEX-4 is not directly connected to the intermediate cycle heat exchange system, variations in ϕ exert only an indirect influence on its performance. As demonstrated in Fig. 16(a), although the air-side temperature difference across HEX-4 exhibits a peak, the maximum variation is merely 1.9 K, indicating that the effect of ϕ on HEX-4 is minimal. Fig. 16(b) illustrates the changes in heat transfer rate across each HEX. As ϕ increases, Q_1 rises rapidly at first and then gradually plateaus, while Q_2 increases slowly before declining sharply, following trends consistent with their respective air-side temperature difference curves. As a result of the combined behavior of Q_1 and Q_2, the total heat transfer rate Q_3 initially increases and then decreases, reaching a maximum of 3630 kW at $\phi =$ 0.7. In contrast, Q_4 is only marginally affected by changes in ϕ, exhibiting minimal variation. Fig. 16 indicates that there exists an optimal distribution ratio of the intermediate working fluid mass flow rate that maximizes the heat transfer capacity of the intermediate cycle heat exchange system. In the experimental study of multi-branch intermediate cycle heat exchange systems conducted by Liu et al. [26]., a similar phenomenon was observed, namely that there exists an optimal flow distribution ratio that maximizes the system heat transfer. This further validates the reliability of the results obtained in the present study.

Fig. 17(a) displays the relationship between ϕ and temperatures T_7 and $T_{6.1}$. $T_{6.1}$ initially increases and then decreases, reaching a maximum of 283.0 K at $\phi = 0.7$, which is the same as the optimal point identified in Fig. 16(b). In contrast, T_7 initially decreases and then plateaus, with a relatively small overall variation—declining from 1842.8 K

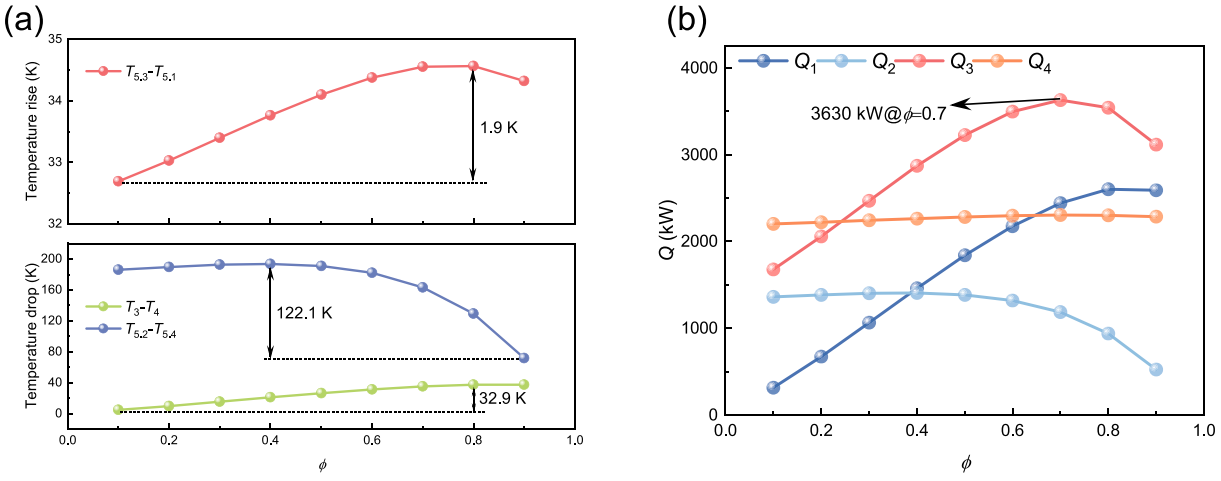

Fig. 16. Effect of the distribution ratio of helium flow in branches ϕ on (a) temperature drop or rise on the air side of the HEXs within the system; (b) heat transfer rate of different HEX.

to 1803.4 K. The plot in Fig. 17(b) indicates W_{HPC} decreases initially and then plateaus with increasing ϕ. Both F_s and η_{th} exhibit a non-monotonic trend, increasing to a peak and subsequently declining. However, the magnitudes of these variations are relatively small, similar to the observations reported in Section 4.3. Based on the above analysis, it is evident that an optimal ϕ exists, enabling the intermediate cycle heat exchange system to operate under near-optimal conditions. This is because ϕ directly controls the relative effectiveness of HEX-1 and HEX-2. Since HEX-1 generally handles a larger heat load than HEX-2, a larger share of helium flow to this branch improves overall heat transfer and reduces compressor work. However, excessive allocation to HEX-1 deprives HEX-2 of cooling capacity, limiting the effectiveness of turbine cooling air and reducing system efficiency. The optimum $\phi = 0.7$ therefore reflects a well-balanced allocation that maximizes the total heat transfer rate of the intermediate cycle and yields the highest hydrogen preheat temperature. Although the improvement in propulsion performance is relatively limited, it remains beneficial. Moreover, dynamically adjusting ϕ in response to changing flight conditions allows the system to meet varying thermal management demands. For example, under high-thrust conditions, a reduced ϕ increases Q_2, thereby enhancing the cooling of turbine cooling air. Conversely, during the cruise, a higher ϕ increases Q_1, improving intercooling and enhancing overall thermal efficiency. These findings underscore the importance of adaptive flow distribution strategies in achieving balanced and efficient thermal management for hydrogen-fueled turbofan engines.

Although the intermediate helium loop proves effective in the present thermodynamic model, its application in real engines will face challenges related to added system weight, increased piping, and higher integration complexity. These drawbacks must be balanced against the safety and stability advantages of avoiding direct contact between cryogenic hydrogen and high-temperature air. Alternative configurations, such as simplified direct heat exchange or cascaded multifluid systems, could potentially reduce system weight and complexity, but at the expense of safety margins or heat exchange effectiveness. Future studies will therefore need to evaluate these trade-offs by combining thermodynamic performance with weight, safety, and integration assessments.

5. Conclusions

This study establishes a synergistic heat recoverydissipation architecture for hydrogen turbofan engines, underpinned by a heat current modeling framework that integrates an intermediate-cycle helium loop with a phase-change-coupled LH_2 preheating process. Parametric analyses of key thermodynamic variables—including bypass ratio (B), turbine inlet temperature (T_7), helium mass flow rate (m_{12}), and distribution ratio of helium flow in branches (ϕ)—yields a comprehensive thermodynamic performance map to guide energy-efficient configuration selection. The results demonstrate the feasibility and effectiveness of applying energy flow topology–based modeling to the design and optimization of advanced aero-engine TMSs, offering valuable insights for the development of zero-emission propulsion technologies. The key findings can be summarized as follows.

i. The proposed energy-flow-oriented thermal modeling approach for hydrogen-fueled aviation engines leverages Kirchhoff's voltage law to eliminate redundant computational intermediates, thereby enabling efficient analysis of complex nonlinear thermal behaviors within the system. The model exhibits high predictive accuracy, with a maximum temperature deviation of 23.15 K, demonstrating its reliability for system-level thermodynamic evaluations.
ii. There exists an optimal bypass ratio of $B = 2.4$, at which the engine achieves its maximum thermal efficiency of 0.507. However, both the *SFC* and *SFCR* increase with a rising bypass ratio, indicating that a higher design bypass ratio may adversely affect the engine's economic performance despite improvements in thermal efficiency.
iii. An increase in turbine inlet temperature (T_7) positively influences the system by enhancing the heat transfer rate across all HEXs, reducing HPC power consumption, and improving both η_{th} and F_s. As T_7 increases from 1550 K to 2200 K, F_s rises from 648.2 (N·s)/kg to 914.3 (N·s)/kg. However, this thermal performance improvement comes at the cost of deteriorating economic performance.
iv. The helium mass flow rate (m_{12}) can regulate the heat transfer capacity of the intermediate cycle heat exchange system, but its effect exhibits diminishing returns. When m_{12} exceeds 1.4 kg/s, the system becomes increasingly insensitive to further increases. A lower m_{12} provides multiple advantages for the thermodynamic performance of the engine, including more efficient thermal energy utilization, a higher preheated hydrogen temperature, and improved F_s and η_{th}.
v. The optimal distribution ratio of helium flow in branches is identified to be $\phi = 0.7$, at which the intermediate cycle heat exchange system achieves its maximum heat transfer capacity and preheated hydrogen temperature ($T_{6.1}$), reaching 3630 kW and 283.0 K, respectively. This operating point reflects a well-balanced allocation of thermal load between the intercooler

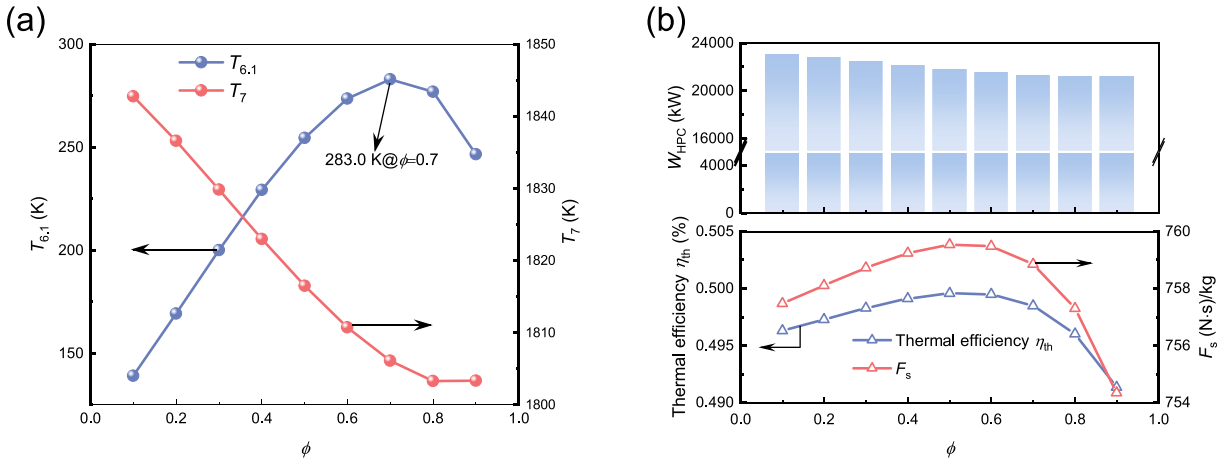

Fig. 17. Effect of the distribution ratio of helium flow in branches ϕ on (a) turbine inlet temperature T_7 and preheated hydrogen temperature $T_{6.1}$; (b) thermal efficiency, specific thrust, and HPC power consumption.

and CCA cooler, thereby maximizing the overall thermal efficiency and effectiveness of the heat exchange process.

It is important to note that the present study primarily concentrates on steady-state theoretical thermodynamic analysis. In practice, weight and size constraints limit the feasible heat transfer area of HEXs, which in turn affects the *KA* values used in the model and may reduce the heat transfer rate and hydrogen preheated temperature. Integration challenges, such as pipeline arrangement and the installation of additional components, may further lower overall efficiency and the thrust-to-weight ratio. Other practical aspects, including distributed losses and dynamic response behaviors, are also beyond the scope of this work and will be systematically addressed in future research.

As a next step, we will undertake targeted experimental validation to ground and extend the model. Because engine-level testing is resource-intensive, validation will focus on a cryogenic intermediate cycle heat exchange experimental system employing air, helium, and liquid nitrogen as working fluids. In the initial phase, liquid nitrogen will serve as a safe surrogate for liquid hydrogen given its flammability and explosion hazards. The facility will provide mass flow rate, temperature, and pressure data across a range of operating conditions to assess model fidelity and characterize the system's dynamic behavior under transient loads.

CRediT authorship contribution statement

Weitong Liu: Writing – original draft, Software, Methodology, Investigation, Formal analysis, Data curation. **Guoqiang Xu:** Supervision, Conceptualization. **Xiuting Gu:** Resources. **Yiang Liu:** Resources. **Jiayang Wang:** Resources. **Jingzhi Zhang:** Writing – review & editing. **Yanchen Fu:** Writing – review & editing, Project administration, Funding acquisition.

Declaration of competing interest

The authors declare that they have no known competing financial interests or personal relationships that could have appeared to influence the work reported in this paper.

Acknowledgment

The authors appreciate the supports from the Beijing Nova Program (No. 20240484560), Beijing Municipal Science & Technology Commission, Administrative Commission of Zhongguancun Science Park (No. Z241100007424005), and the Academic Excellence Foundation of BUAA for PhD Students.

Data availability

Data will be made available on request.

References

[1] Ebrahimi A, Rolt A, Jafari S, Anton JH. A review on liquid hydrogen fuel systems in aircraft applications for gas turbine engines. Int J Hydrogen Energ 2024;91:88–105.
[2] Gg F, I dLe, R S. Environmental trends in aviation to 2050 background. https://www.icao.int/environmental-protection/Documents/EnvironmentalReports/2019. International Civil Aviation Organization. 10 July 2023.
[3] Oesingmann K, Grimme W, Scheelhaase J. Hydrogen in aviation: a simulation of demand, price dynamics, and CO2 emission reduction potentials. Int J Hydrogen Energ 2024;64:633–42.
[4] Lemmon E, Huber ML, McLinden MO. NIST standard reference database 23: reference fluid thermodynamic and transport properties-REFPROP. 2007. version 8.0.
[5] Liu P, Yang T, Zheng H, Huang X, Wang X, Qiu T, et al. Thermodynamic analysis of power generation thermal management system for heat and cold exergy utilization from liquid hydrogen-fueled turbojet engine. Appl Energy 2024;365.
[6] Berg F, Palmer J, Miller P, Dodds G. HTS system and component targets for a distributed aircraft propulsion system. IEEE Trans Appl Supercond 2017;27(4):1–7.
[7] Dong P, Tang H, Chen M. Study on multi-cycle coupling mechanism of hypersonic precooled combined cycle engine. Appl Therm Eng 2018;131:497–506.
[8] Capitao Patrao A, Jonsson I, Xisto C, Lundbladh A, Lejon M, Grönstedt T. The heat transfer potential of compressor vanes on a hydrogen fueled turbofan engine. Appl Therm Eng 2024:236.
[9] Abedi H, Xisto C, Jonsson I, Grönstedt T, Rolt A. Preliminary analysis of compression system integrated heat management concepts using LH2-Based parametric gas turbine model. Aerospace-Basel 2022;9(4).
[10] Wen J, Wan C, Xu G, Zhuang L, Dong B, Chen J. Optimization of thermal management system architecture in hydrogen engine employing improved genetic algorithm. Energy 2024;297.
[11] Srinath AN, Pena López Á, Miran Fashandi SA, Lechat S, di Legge G, Nabavi SA, et al. Thermal management system architecture for hydrogen-powered propulsion technologies: practices, thematic clusters, system architectures, future challenges, and opportunities. Energies 2022;15(1).
[12] Tiwari S, Pekris MJ, Doherty JJ. A review of liquid hydrogen aircraft and propulsion technologies. Int J Hydrogen Energ 2024;57:1174–96.
[13] Norris G. Pratt outlines hydrogen steam-injection engine concept. Aviat Week Space Technol April. 2022;19.
[14] Wang X, He A, Hu Z. Transient modeling and performance analysis of hydrogen-fueled aero engines. Processes 2023;11(2).
[15] Aerospace Technology Institute. FlyZero. https://www.ati.org.uk/flyzero/.AerospaceTechnologyInstitute. [Accessed 27 January 2023].
[16] Webber H, Llambrich J, Davoudi H. FlyZero: thermal management roadmap report. Aerospace Technology Institute; 2022. https://www,ati.org.uk/wp-content/uploads/2022/03/FZO-PPN-COM-0019-Thermal-Management-Roadmap-Report.pdf.
[17] Haglind F, Singh R. Design of aero gas turbines using hydrogen. J Eng Gas Turbines Power 2004;128(4):754–64.
[18] Patrao AC, Jonsson I, Xisto C, Lundbladh A, Grönstedt T. Compact heat exchangers for hydrogen-fueled aero engine intercooling and recuperation. Appl Therm Eng 2024:243.
[19] Seitz A, Nickl M, Troeltsch F, Ebner K. Initial assessment of a fuel cell—gas turbine hybrid propulsion concept. Aerospace-Basel 2022;9(2).
[20] Balli O, Ozbek E, Ekici S, Midilli A, Hikmet Karakoc T. Thermodynamic comparison of TF33 turbofan engine fueled by hydrogen in benchmark with kerosene. Fuel 2021;306.
[21] Akdeniz HY, Balli O. Impact of different fuel usages on thermodynamic performances of a high bypass turbofan engine used in commercial aircraft. Energy 2022;238.
[22] Oğur E, Koç A, Köse Ö, Yağlı H, Koç Y. Energy, exergy, exergoeconomic, exergy sustainability and exergoenvironmental analyses (5E) of a turbofan engine: a comparative study of hydrogen and kerosene fuels. Fuel 2025;381.
[23] Oğur E, Koç A, Yağlı H, Koç Y, Köse Ö. Thermodynamic, economic, and environmental analysis of a hydrogen-powered turbofan engine at varying altitudes. Int J Hydrogen Energ 2024;55:1203–16.
[24] Derakhshandeh P, Ahmadi A, Dashti R. Simulation and technical-economic-environmental optimization of the general electric GE90 hydrogen turbofan engine. Int J Hydrogen Energ 2021;46(5):3303–18.
[25] Lieuwen TC, Yang V. Combustion instabilities in gas turbine engines. 2006.
[26] Liu W, Xu G, Gu X, Yao J, Li M, Lei M, et al. Experimental analysis and thermodynamic modeling for multilevel heat exchange system with multifluid in aero engines. Energy 2025;315.
[27] Liu W, Xu G, Zhi H, Wang R, Li M, Fu Y. Experimental evaluation of hydrothermal performance in airfoil-fin PCHE with supercritical pressure hydrocarbon fuel. Int Commun Heat Mass Tran 2024;159.
[28] Noton M, Swinerd G. Optimization of the rocket-powered ascent of Hotol. Acta Astronaut 1989;19(1):17–26.
[29] Aggarwal R, Lakhara K, Sharma P, Darang T, Jain N, Gangly S. Sabre engine: single stage to orbit rocket engine. Int J Innov Res Sci Eng Technol 2015;4(10):10360–6.
[30] Zhang J, Wang Z, Li Q. Thermodynamic efficiency analysis and cycle optimization of deeply precooled combined cycle engine in the air-breathing mode. Acta Astronaut 2017;138:394–406.
[31] Longstaff R, Bond A. The SKYLON project. Conference the SKYLON project. p. 2244.
[32] Zhou J, Lu H, Zhang H, Zhao L, Chen J, Zheng R. A preliminary research on a two-stage-to-orbit vehicle with airbreathing pre-cooled hypersonic engines. 21st AIAA international space planes and hypersonics technologies Conference2017.
[33] Wang C, Yu X, Pan X, Qin J, Huang H. Thermodynamic optimization of the indirect precooled engine cycle using the method of cascade utilization of cold sources. Energy 2022;238.
[34] Ang EYM, Ng PS, Soh CB, Wang PC. Multi-stage thermoelectric coolers for cooling wearables. Therm Sci Eng Prog 2022;36.
[35] Liu W, Xu G, Gang X, Qi H, Li M, Wen J, et al. Theoretical modeling, experimental validation, and thermodynamic analysis on intermediate heat-exchange cycle system. Int Commun Heat Mass Tran 2024;156.
[36] Fu Y, Liu W, Qi H, Chen Q, Wen J, Xu G. Heat transfer area optimization of intermediate heat-exchange cycle system for aero engines. Int J Heat Mass Tran 2024;220.
[37] Liu J, Wang S, Zhang T, Wang Y, He K, Cui Z, et al. Experiment and simulation on a thermal management scheme of intermediate circulation based on heat current method. Int J Heat Mass Tran 2023;206.
[38] Liu J, Li M, Zhang T, Wang Y, Cao Z, Shao W, et al. Optimization of the aero-engine thermal management system with intermediate cycle based on heat current method. Appl Therm Eng 2024:237.

[39] Jiang T, Zhan T-T, Li Y-H, Yang K, He N, Wang N, et al. Heat transfer characteristics and flow distribution behavior of pyrolytic ammonia in scramjet regenerative cooling channels. Energy 2025;335.
[40] Colera M, Soria Á, Ballester J. A numerical scheme for the thermodynamic analysis of gas turbines. Appl Therm Eng 2019;147:521–36.
[41] Kamath RS, Biegler LT, Grossmann IE. An equation-oriented approach for handling thermodynamics based on cubic equation of state in process optimization. Comput Chem Eng 2010;34(12):2085–96.
[42] Arnold M. Stability of sequential modular time integration methods for coupled multibody system models. J Comput Nonlinear Dynam 2010;5(3).
[43] Chen Q, Hao J, Zhao T. An alternative energy flow model for analysis and optimization of heat transfer systems. Int J Heat Mass Tran 2017;108:712–20.
[44] Chen Q. Entransy dissipation-based thermal resistance method for heat exchanger performance design and optimization. Int J Heat Mass Tran 2013;60:156–62.
[45] Zhao T, Chen X, He K-L, Chen Q. A standardized modeling strategy for heat current method-based analysis and simulation of thermal systems. Energy 2021;217.
[46] Liang Z, Zhao T, Ma H, Chen Q, Wang S. An isomorphic multi-energy circuit analysis method for multi-stack SOFC systems considering nonlinear electrochemical reaction and gas transport. Appl Energy 2025;377.
[47] Zhao T, Min Y, Chen Q, Hao J. Electrical circuit analogy for analysis and optimization of absorption energy storage systems. Energy 2016;104:171–83.
[48] He K, Zhao T, Chen Q, Chen X. Matrix-based network heat transfer modeling approach and its application in thermal system analysis. Appl Therm Eng 2020;181.
[49] Cao M, Wang Z, Tang H, Li S, Ji Y, Han F. Heat flow topology-driven thermo-mass decoupling strategy: Cross-scale regularization modeling and optimization analysis. Appl Energy 2024;367.
[50] Wang Z, Cao M, Tang H, Ji Y, Han F. A global heat flow topology for revealing the synergistic effects of heat transfer and thermal power conversion in large scale systems: methodology and case study. Energy 2024;290.
[51] Fu Y, Liu W, Wang J, Zhang L, Wen J, Wu H, et al. Experimental investigation on heat transfer enhancement of supercritical pressure aviation kerosene in tubular laminar flow by vibration. Appl Therm Eng 2024;257.
[52] Liu W, Xu G, Fu Y, Wen J, Zhang N. Numerical investigation on forced, natural, and mixed convective heat transfer of n-decane in laminar flow at supercritical pressures. Int J Heat Mass Tran 2023;209.
[53] Zhuang L, Xu G, Liu Q, Li M, Dong B, Wen J. Superiority analysis of the cooled cooling air technology for low bypass ratio aero-engine under typical flight mission. Energy Convers Manag 2022;259.
[54] Adolfo D, Bertini D, Gamannossi A, Carcasci C. Thermodynamic analysis of an aircraft engine to estimate performance and emissions at LTO cycle. Energy Proc 2017;126:915–22.
[55] Balli O. Exergy modeling for evaluating sustainability level of a high by-pass turbofan engine used on commercial aircrafts. Appl Therm Eng 2017;123:138–55.
[56] Bell IH, Wronski J, Quoilin S, Lemort V. Pure and pseudo-pure fluid thermophysical property evaluation and the open-source thermophysical property library CoolProp. Ind Eng Chem Res 2014;53(6):2498–508.
[57] Xu W, Li Q, Huang M. Design and analysis of liquid hydrogen storage tank for high-altitude long-endurance remotely-operated aircraft. Int J Hydrogen Energ 2015;40(46):16578–86.
[58] Razi F, Dincer I, Gabriel K. A specific exergy costing assessment of the integrated copper-chlorine cycle for hydrogen production. Int J Hydrogen Energ 2020;45(56):31425–39.